Citation
Cheng, R. and Chen, W. and Hao, H. and Li, J. 2022. Dynamic response of road tunnel subjected to internal Boiling liquid expansion vapour explosion (BLEVE). Tunnelling and Underground Space Technology. 123: ARTN 104363.
http://doi.org/10.1016/j.tust.2022.104363

Dynamic response of road tunnel subjected to internal Boiling Liquid Expansion Vapour Explosion (BLEVE)

Ruishan Cheng, Wensu Chen*, Hong Hao*, Jingde Li

Center for Infrastructural Monitoring and Protection, School of Civil and Mechanical Engineering, Curtin University, Australia

*Corresponding authors: wensu.chen@curtin.edu.au (Wensu Chen), Hong.Hao@curtin.edu.au (Hong Hao)

Abstract: During service life, road tunnels may face threats of accidental explosions, e.g., Boiling Liquid Expansion Vapour Explosions (BLEVEs) due to accidents of vehicles transporting hazardous goods inside the tunnels. However, very limited study has investigated the influence of BLEVEs inside a tunnel on its dynamic response. The present study numerically investigates the dynamic response of an arched tunnel subjected to an internal BLEVE by using the software LS-DYNA. The BLEVE load is directly simulated by using commercial code FLACS or approximated by the commonly used TNT equivalency method to investigate the influences of loading predictions on the tunnel responses. The results show that the corner and upper arc of arched lining are more prone to be damaged under the directly predicted BLEVE loads. Compared to the directly predicted BLEVE loads, explosion loads estimated by the TNT equivalency method induce more significant damage to the lining due to its higher peak pressure, but smaller peak displacements since the corresponding impulse is lower than that of the BLEVE load. In addition, parametric studies are conducted to investigate the effects of concrete grade, concrete thickness, steel reinforcement ratio, and stiffness of surrounding rock mass on dynamic response of the arched tunnel subjected to the internal BLEVE. It is found that increasing concrete grade and thickness and enhancing the stiffness of

surrounding rock mass are more effective than increasing steel reinforcement ratio in improving the performance of the arched tunnel against internal BLEVE loadings.

Keyword: Tunnel; Boiling Liquid Expansion Vapour Explosion (BLEVE); Structural response; Numerical study

1. Introduction

Road tunnels as important parts of modern road systems have been gaining popularity by virtue of their advantages in overcoming terrain obstacles and reducing environmental impacts (Cheng et al., 2021; Mussa et al., 2017). Road tunnels during service life may experience internal accidental explosion loads such as those from Boiling Liquid Expansion Vapour Explosions (BLEVEs) due to accidental rupture of transported gas tankers or high explosive (HE) explosions owing to terrorist activities. These internal explosions may lead to severe damage to tunnel structures. Cheng et al. (2021) summarised typical tunnel internal explosion accidents and tunnel damage related to HE explosions and BLEVEs. Existing design codes and guidelines of road tunnels such as AGRT02-19 (Austroads, 2019) in Australia, JTG 3370.1-2018 (Ministry of Transport of the People's Republic of China, 2018) in China, and FHWA-NHI-10-034 (US Department of Transportation Federal Highway Administration, 2009) in the USA only consider static loads (e.g., the overburden of tunnels and the self-weight of structures, etc.) seismic loads, and heat loads, etc., but not blast loads. As road tunnels may experience internal explosion loads as reviewed in Cheng et al. (2021), it is necessary to understand the performance of road tunnels subjected to such loads for tunnel safety and to conduct effective blast-resistant designs of road tunnels to minimize the loss of life and economy and the disruption of transportation network.

Many studies have experimentally, numerically, and analytically investigated the dynamic response and structural damage of tunnels subjected to internal HE explosions. Gao et al. (2013) used Laplace transform to analytically solve the displacement and stress on tunnel linings as well as the pore pressure at lining-soil interfaces under internal explosion-like impulsive loads. It was found that increasing lining thickness significantly decreased the dynamic response of tunnels, while additional pore fluid mass in soil surroundings substantially increased the hoop stress and radial displacement of tunnel structures. However, the analytical method was based on the elastic wave theory, which can hardly be used to estimate the real tunnel damage subjected to high-intensity internal explosions. Krone (2018) conducted scaled-down explosion tests to investigate the damage modes of circular tunnels subjected to internal explosions of composition-C (C4) charge. The test results clearly showed that hoop and longitudinal cracks on the concrete of RC linings were formed near explosions, wherein the hoop cracks were surrounded by multiple longitudinal cracks. Zhou (2011) conducted full-scale tests of TNT explosions inside tunnel-like underground rock chambers without the support of RC linings. The test results indicated that ten craters with similar sizes were formed on the floor below ten detonated charges. No rock fall from the roof or sidewalls was observed, which was attributed to the energy-absorbing of shotcretes on the roof and sidewalls, as well as the small explosive quantities used in the tests. It is worth noting that tunnel explosion experiments are of high-risk, time-consuming and expensive, thereby limiting their popularity in research and development (R&D).

Owing to the aforementioned shortcomings of theoretical and experimental methods, numerical simulation as a popular alternative for predictions of tunnel responses under internal explosions has been widely conducted in the existing studies. For example, Feldgun et al. (2014) numerically investigated the dynamic response of rectangular tunnel linings subjected to internal centric and eccentric explosions by the coupled Godunov-variational difference method (VDM). Compared to centric explosions, eccentric explosions not only induced more severe response to closer walls of tunnels, but also caused more obvious response to distant walls of tunnels due to intensive blast waves reflecting from the closer walls. Kristoffersen et al. (2019) used the Lagrangian method to investigate dynamic response of circular and rectangular tunnels subjected to internal eccentric explosions. The results revealed that the circular tunnel would be preferable to the rectangular tunnel because the circular geometry contributed to more evenly distributed strains in tunnel linings than rectangular tunnels. Tiwari et al. (2016) investigated the dynamic response of circular tunnels with three weathering levels of rock surroundings (i.e., rock surroundings with high, moderate and low elastic moduli) under internal TNT explosions by using the coupled Eulerian–Lagrangian (CEL) method. The results showed that the high-weathering rock tunnel, i.e., tunnel with low-modulus rock surroundings subjected to internal HE loadings experienced the most severe damage among the three types of rock tunnels.

Compared to HE explosions, BLEVEs with the same energy release tend to generate blast waves with lower peak pressure, slower rising time, longer duration and higher impulses (Hao et al., 2016). Therefore, the dynamic responses of road tunnels subjected to BLEVEs are different from those subjected to HE explosions. In open literature, only two studies (Molenaar et al., 2009; Vervuurt et al., 2007) numerically investigated the dynamic response of a multi-cell rectangular tunnel subjected to internal BLEVEs. Free-field BLEVE loads were applied to tunnel structures without considering the interactions between blast waves and tunnel structures, which might underestimate the structural response of tunnels subjected to internal BLEVEs because confinement and pressure wave interaction with tunnel are likely to enhance the blast loads acting on the tunnel. Therefore, it is essential to investigate the dynamic response of road tunnels subjected to internal BLEVEs. Furthermore, because it is not straightforward to estimate BLEVE loads, simplified methods such as TNT equivalency method is commonly used in research and design analyses to approximate BLEVE loads. It is also interesting to understand the reliability and accuracy of tunnel structural responses obtained by using explosion load estimated by TNT equivalency method in representing the BLEVE load.

In the present study, the dynamic response of an arched road tunnel subjected to an internal BLEVE is numerically investigated by using the software LS-DYNA. The internal BLEVE loads are simulated by the computational fluid dynamic (CFD) software-FLACS. The overpressure prediction accuracy of FLACS has been validated by the authors (Li and Hao, 2020). The lining and rock surroundings of the arched tunnel in the numerical model are calibrated by using the existing test results of RC slab and tunnel-like rock chamber subjected to TNT explosions, respectively. With the calibrated numerical model, the damage mode and dynamic response of arched tunnel against the internal BLEVE are investigated and compared with those subjected to its equivalent HE explosion load estimated with a TNT equivalency method. In addition, parametric studies are conducted to investigate the effects of concrete grade, concrete thickness, steel reinforcement ratio, and surroundings stiffness on the dynamic response and damage mode of the arched tunnel subjected to internal BLEVEs.

2. Numerical model

2.1 Geometric configuration and finite element model

A typical arched tunnel, namely Qidaoliang tunnel in China (Lai et al., 2016) with the inner cross-sectional dimension of 10.8m (span) × 7.1m (height) is used for the case study. Due to the symmetry of the arched tunnel about *xy* and *yz* planes, only a quarter of the arched tunnel is included in the numerical model (see **Figure 1**(a)), which is composed of tunnel linings and rock surroundings. The half cross section of the arched tunnel comprises of an upper quarter circle (i.e., the upper arc) with the radius of 5.4 m and a lower arc with the radius of 7.9 m, as shown in **Figure 1**(b). The centre of the quarter circle (i.e., the upper arc) is 1.7 m from the tunnel floor. The tunnel linings are made of composite linings, i.e., first lining and secondary lining. The first lining is shotcrete with a thickness of 100 mm. The secondary lining consists of cast-in-place concrete with a thickness of 500 mm for the arched lining and a maximum thickness of 1.5 m for the invert of tunnel. The 20 mm-diameter steel rebars are arranged in forms of double layers for secondary lining along the length of tunnel with the spacing of 200 mm for longitudinal rebars, hoop rebars, and shear rebars, respectively, as shown in **Figure 1**(c).

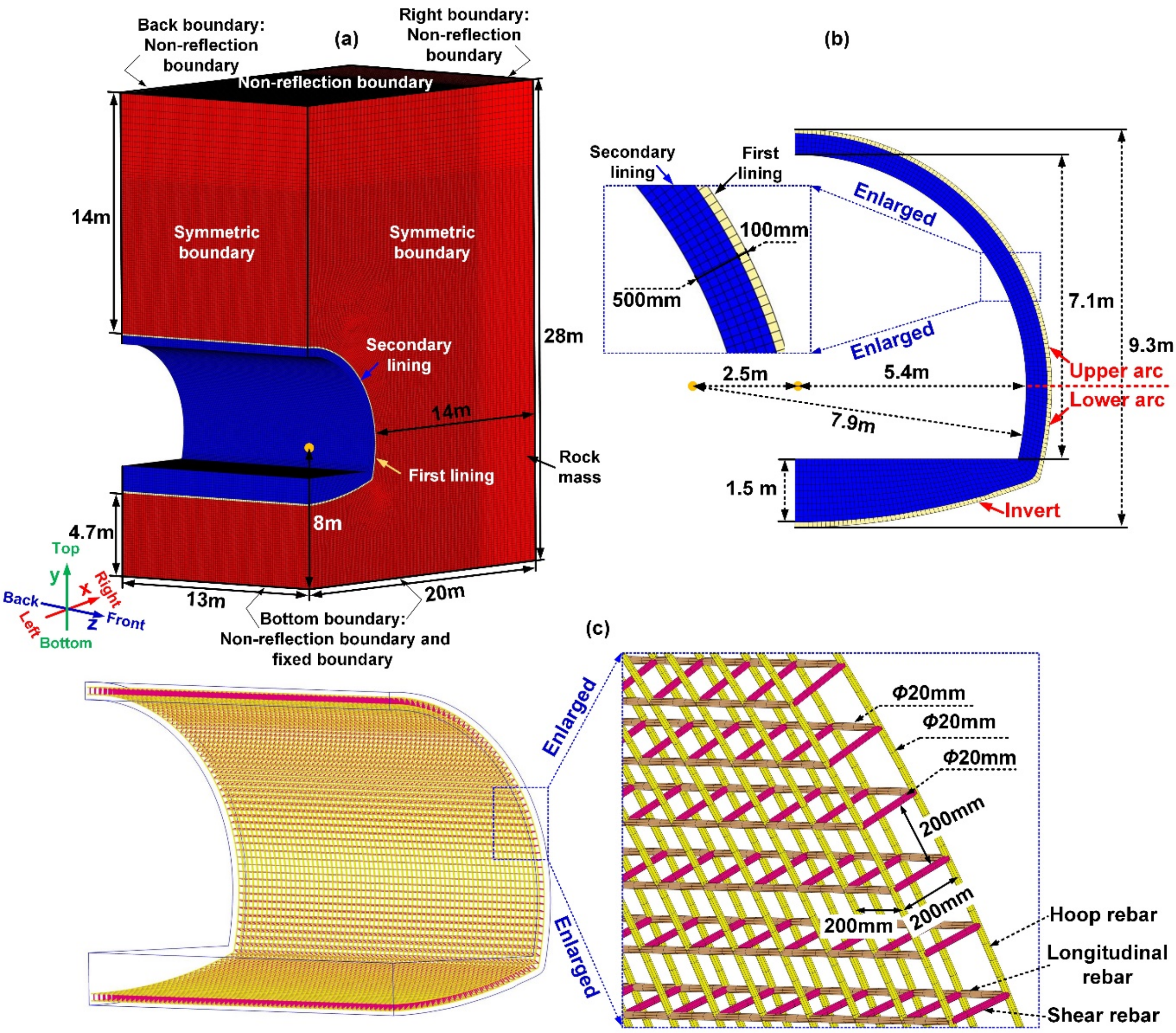

Figure 1. The geometric configuration and boundary setting of the numerical model, (a) the overall numerical model and boundary conditions, (b) lining configuration, (c) steel rebar configuration.

Symmetric boundaries are applied to the front and left surfaces of the numerical model (see **Figure 1**(a)). Since the considered tunnel is an underground tunnel with a relatively large cover depth, the partial cover depth of tunnel instead of the entire cover depth of tunnel up to the ground surface is included in the model. Non-reflecting boundary is assigned to the right plane, the back plane, the bottom plane, and the top plane as indicated in **Figure 1**(a). A fixed boundary condition is also applied to the bottom plane to prevent the whole model from moving along *y* direction (i.e., vertical direction) under BLEVE loads. It is noted that non-reflecting boundaries cannot completely eliminate the reflection of stress waves from the boundaries. Therefore, a sufficient model domain is deemed necessary to minimize the influence of reflected stress waves with acceptable computational cost. In this study, the effect of boundary reflections has been examined through domain convergence tests as also performed in Chaudhary et al. (2018), i.e., comparing the damage and response of tunnel by reducing model domains. After conducting the domain convergence analyses, the effective domain sizes adopted in the numerical model are set as 20 m (width) × 28 m (height) × 13 m (length), as shown in **Figure 1**(a).

All steel rebars modelled by beam elements are constrained in the solid concrete elements by employing the keyword *CONSTRAINED_BEAM_IN_SOLID in LS-DYNA. The stiffness-based hourglass control is applied by using the keyword *CONTROL_HOURGLASS in LS-DYNA to overcome hourglass effects of solid elements with single integration point, which is used for the concrete of tunnel lining and rock surroundings in the present numerical model. The hourglass coefficient is set as 0.05 to ensure the maximum hourglass energy less than 5% of total energy in the numerical model. The element size should be less than 1/12th of the wavelength of stress waves (i.e., the ratio of wave velocity and frequency) in numerical modelling (Blair, 2015). The maximum element size around the tunnel is calculated as 183 mm in this study since the wave velocities in concrete and rock mass are no less than 2200 m/s based on the formula of stress wave velocity specified in Cotsovos et al. (2008) and the main frequencies of BLEVE loads are below 1000 Hz. In the present study, the mesh size of 100 mm and 50 mm are utilized for the concrete elements of arched lining and the steel rebar elements, respectively. It is noted that the mesh size of solid elements around the tunnel (i.e., 100 mm) is determined by comparing the strain energies of lining in three cases with the mesh sizes of 50 mm, 100 mm, and 200 mm. To improve the calculation efficiency, the mesh size of rock mass gradually changes from 100 mm to 450 mm with the increased distance away from the tunnel lining.

In engineering practice, anchor rods or rock bolts are often used to strengthen the damaged rock mass near the excavated tunnel, which ensures the stability of rock mass. In this study, the safety of the lining is focused, and the surrounding rock mass of the tunnel is assumed as undamaged in the numerical model. Therefore, the rock bolts anchored in rock mass are not considered in the simulation. In addition, the surrounding rock mass of the tunnel in this study is relatively intact based on the site investigation (Yang, 2006). The mechanical properties of the rock mass are given in Table 2 of Section 2.3.2. It should be noted that the cover depth of the shallow tunnel considered in this study is not greater than 50 m and the in-situ stress of rock mass around the tunnel is relatively low. As compared to the intensive explosion loads, in-situ stress has very limited influence on the dynamic response of the tunnel subjected to internal explosions. Therefore, in-situ stress is not considered in this study for simplicity.

2.2 BLEVE loads

A BLEVE is defined as the physical explosion resulting from vapour expansion and violent boiling of the pressurized superheated liquid (i.e., liquid flashing) in a container that suddenly fails (Birk et al., 2019; Li and Hao, 2020). The BLEVE of flammable materials (e.g., liquefied petroleum gas (LPG)) can generate an intensive blast overpressure and the ground loading with the projectile of vessel fragments at a high velocity, a violent phase change destroying a vessel, a high-speed ejection of a two-phase mixture, and potential fireballs (Birk et al., 2019; Eyssette et al., 2021). Tunnel structures can be damaged by the combined action of the above hazards. Amongst, the BLEVE overpressure is deemed to be the most significant factor for tunnel damage. However, the specific effect of the BLEVE overpressure on the tunnel response is unclear and thus needs to be comprehensively investigated. In addition, the explosion scenario in which a BLEVE is followed by a confined vapour cloud explosion (VCE) may occur in extreme cases if the flammable material in a vessel is ignited (Eyssette et al., 2021). Compared to the sole BLEVE, the combined BLEVE and VCE explosion could generate a more intensive blast overpressure and hence induce more severe tunnel damage. However, understanding the tunnel behaviour under the BLEVE overpressure is essential prior to the investigation of tunnel response subjected to the combined overpressure of BLEVE and VCE. Therefore, structural response of the tunnel subjected to BLEVE overpressure is focused in the study.

The BLEVE of a typical 20 m^3 liquefied petroleum gas (LPG) cylindrical-like tanker is assumed to occur in the middle of the arched tunnel. In the worst scenario, only 20% of the energy of compressed liquid and gas in tanker is dissipated as reported in Bubbico and Marchini (2008). The remaining 80% of energy can be transformed to generate blast waves. Assuming that the explosive evaporation of liquid and the vapour expansion simultaneously occur at the instant of tanker burst (Van den Berg et al., 2006), the source pressure of BLEVE from the 20 m^3 LPG tanker used in this study may reach 50 MPa in the worst scenario based on the pressure-energy calculation equation developed by Strehlow et al. (1979).

The BLEVE loads acting on the arched tunnel are simulated by using computational fluid dynamic (CFD) based software - FLACS. It is worth noting that the burst of a spherical vessel with the same volume as a cylindrical-like LPG tanker transported inside the road tunnel generates a spherical blast wave in FLACS, which neglects the influences of vessel shape and rupture patterns of the LPG tanker. In order to consider the more realistic BLEVE scenarios, a cylindrical LPG tanker with a diameter of 2.4 m and a length of 4.6 m is simulated in this study. The half-length LPG tanker along the z-direction is shown in **Figure 2**, the centre of which is at the same height as the centre of the upper quarter circle of the arched tunnel. For the actual BLEVE hazards, the blast wave induced by the burst of the cylindrical or spherical cross-section of the LPG tanker is neither isotropic nor hemispherical in the near field (Olav and Kjellander, 2016) due to the uncertainty, unevenness, and asymmetry of rupture pattern of LPG tanker. However, for numerical simulations, it is a general practice to model the BLEVE waves as evenly radiated waves by assuming the LPG tankers rupture completely with instantaneous openings (Li and Hao, 2020). The accuracy of the simulated BLEVE loads inside tunnels has been verified in the authors' previous study (Li et al., 2021) and is therefore not repeated here.

This study focuses on investigating the damage of arched lining as it may cause the tunnel collapse. The significant damage of arched lining is mainly caused by the BLEVE loads acting directly on the arched lining. BLEVE loads acting on the tunnel floor have limited influence on the response of arched lining. Therefore, BLEVE loads are only applied to the arched lining instead of the whole cross-sectional lining in the simulation to reduce the domain size of the model and thus save computational cost. In order to obtain the pressure time histories of BLEVE on the arched lining, eight monitoring cross-sections with the interval of 1m are arranged along the length of the tunnel from the centre of LPG tanker (see **Figure 2** (a)). At each monitoring cross-section, six monitoring points are arranged along the inner surface of the arched tunnel, among which four monitoring points (1-4) are evenly placed at the upper quarter circle (i.e., red arc in **Figure 2** (b)). The remaining two monitoring points (5 and 6) are equally spaced on the lower arc (i.e., green arc in **Figure 2** (b)). Due to the equal distance from the centre of LPG tanker to the quarter circle of arched tunnel, the pressure data of the upper four monitoring points at each monitoring cross-section is averaged as the input BLEVE loads acting on the upper quarter circle of the arched tunnel. In addition, although the distances from the centre of LPG tanker to different locations of the lower arc wall are slightly varied, the pressure data at the lower two monitoring points is averaged and used as the input BLEVE loads acting on the lower arc of the arched tunnel. The segment within 0.5 m before and after each monitoring cross-section along the length of tunnel is applied with the BLEVE loads obtained at the corresponding monitoring cross-section (see **Figure 2**(a)). It should be noted that 1m is determined as the interval distance of adjacent monitoring cross sections as it gives reasonable approximation of the BLEVE load variations along the tunnel length. The CFD simulated BLEVE loads at the upper quarter circles and the lower arcs of eight segments of the arched tunnel are shown in **Figure 3**(a) and (b), respectively. The visual results of explosion wave inside the1/4 tunnel at different time instants are shown in **Figure 3**(c).

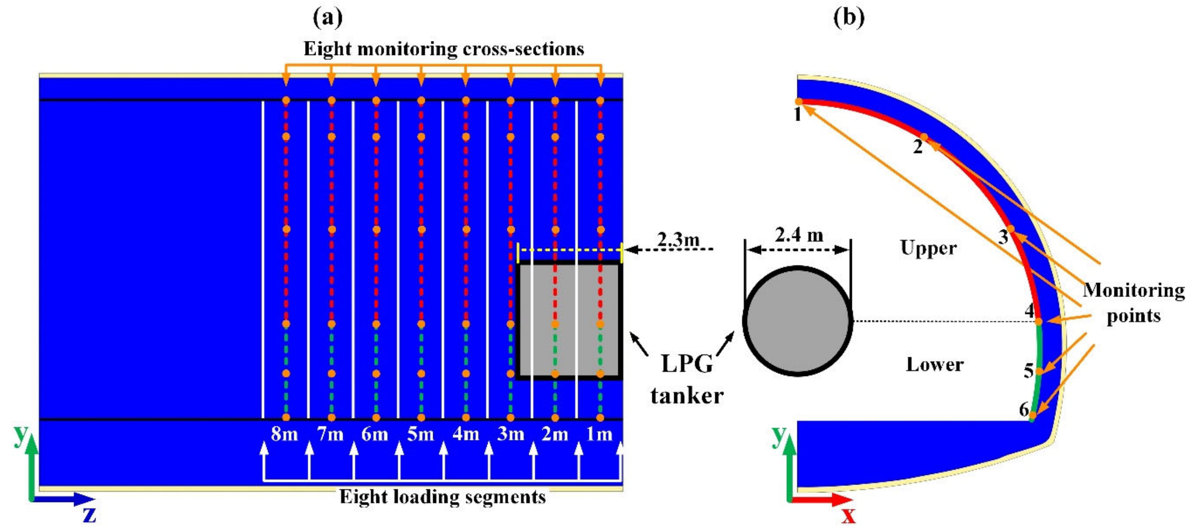

Figure 2. Monitoring arrangement and BLEVE loads on the arched tunnel along (a) tunnel length; (b) cross section

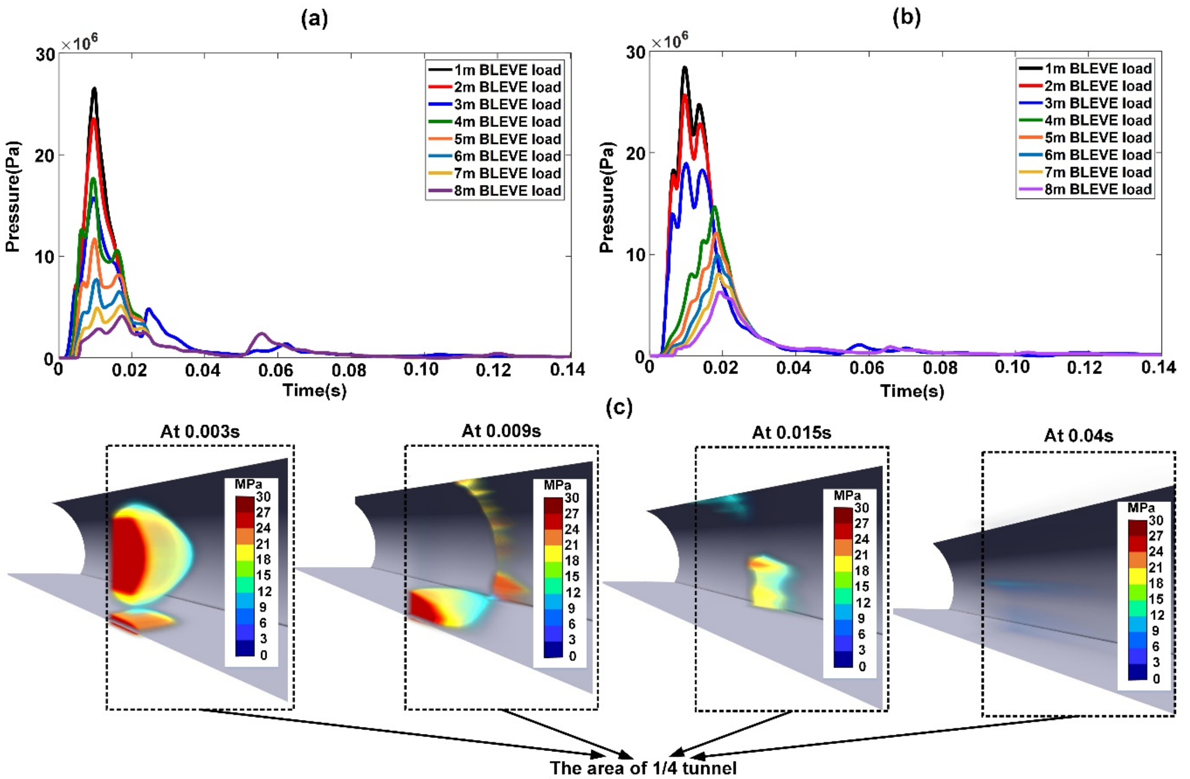

Figure 3. The BLEVE loads applied on (a) upper and (b) lower arcs at eight sections of the arched tunnel, and (c) the visual pressure waves at selected time instants from FLACS.

2.3 Material models

2.3.1 Lining material model

The Karagozian & Case model (i.e., *MAT_CONCRETE_DAMAGE_REL3 or *MAT_72R3 in LS-DYNA) that considers strain hardening, damage, strain softening, and strain rate effect is used to model the concrete of tunnel lining in this study. The accuracy of this material model in simulating the dynamic behaviour of concrete subjected to blast loads has been reported in many previous studies (Chen et al., 2015; Li et al., 2017; Qian et al., 2021a; Qian et al., 2021b). C25 concrete (i.e., concrete with the compressive strength of 25 MPa) is considered in this study, and the basic parameters are listed in **Table 1**. Other material parameters can be generated automatically with the given unconfined compressive strength and unit conversion factors via the built-in algorithm of the material model.

The elastic-plastic material model (i.e., *MAT_PIECEWISE_LINEAR_PLASTICITY, or *MAT_24) is used to model the steel reinforcement of tunnel lining. The typical bilinear strain-stress curves for steel are employed in the model for longitudinal, hoop and shear rebars. **Table 1** gives the material parameters for HRB300 steel rebar (i.e., steel rebar with the yield strength of 300 MPa).

Table 1. Parameters of material model for concrete and steel reinforcement.

Lining component	Material model in LS-DYNA	Parameter	Value
Concrete	*MAT_CONCRETE_DAMAGE_REL3 (*MAT_072R3)	Density	2300 kg/m^3
		Poisson’s ratio	0.2
		Compressive strength	25 MPa
Steel rebar	*MAT_PIECEWISE_LINEAR_PLASTICITY (*MAT_024)	Density	7850 kg/m^3
		Young's modulus	210 GPa
		Poisson’s ratio	0.3
		Yield stress	300 MPa

The concrete and steel rebar are strain-rate dependent and their strength can significantly increase under high strain rates compared to low strain rates. Therefore, it is necessary to consider the strain rate effect for concrete and steel rebar to obtain the accurate structural response of tunnel linings subjected to internal BLEVE loads. The dynamic increase factor (DIF), i.e., the ratio of the dynamic-to-static strength is widely used to represent the strain rate effect on dynamic strength increment. In this study, DIF equations of concrete compressive and tensile strengths (Hao and Hao, 2014) are given in Eqs. (1) and (2), respectively, and DIF equation of yield strength of steel rebar (Malvar, 1998) is expressed in Eq. (3). The keyword * DEFINE_CURVE in LS-DYNA is used to incorporate these relationships of DIF to the corresponding material models of concrete and steel rebar.

$$CDIF_c = \frac{f_{cd}}{f_{cs}} = \begin{cases} 0.0419(\log \dot{\varepsilon}_d) + 1.2165 & \dot{\varepsilon}_d \le 30/s \\ 0.8988(\log \dot{\varepsilon}_d)^2 - 2.8255(\log \dot{\varepsilon}_d) + 3.4907 & \dot{\varepsilon}_d > 30/s \end{cases} \tag{1}$$

$$CDIF_t = \frac{f_{td}}{f_{ts}} = \begin{cases} 0.26(\log \dot{\varepsilon}_d) + 2.06 & \dot{\varepsilon}_d \le 1/s \\ 2(\log \dot{\varepsilon}_d) + 2.06 & 1/s < \dot{\varepsilon}_d \le 2/s \\ 1.44331(\log \dot{\varepsilon}_d) + 2.2276 & 2/s < \dot{\varepsilon}_d \le 150/s \end{cases} \tag{2}$$

$$SDIF = \left(\frac{\dot{\varepsilon}}{10^{-4}}\right)^{0.074 - 0.040\frac{f_y}{414}} \tag{3}$$

where $CDIF_c$, $CDIF_t$, and $SDIF$ are the dynamic increase factor for concrete compressive strength, concrete tensile strength, and yield strength of steel rebar, respectively; f_{cd} and f_{td} are the dynamic compressive strength and dynamic tensile strength of concrete at strain rate $\dot{\varepsilon}_d$; f_{cs} and f_{ts} are the static compressive strength and static tensile strength of concrete; f_y is the steel yield strength in MPa.

2.3.2 Rock material model

The Riedel–Hiermaier–Thoma (RHT) model (i.e., *MAT_RHT or *MAT_272 in LS-DYNA) is employed to simulate the rock mass surrounding the arched tunnel. The equation of state (EOS) of RHT model is defined by the Mie–Greisen form with a polynomial Hugoniot curve and the porosity of material (Cui et al., 2017). Three stress limit surfaces, i.e., initial elastic yield surface, failure surface and residual friction surface with strain rate effects, are included in the RHT model for the strength properties of the rock mass. The damage level of rock mass in the RHT model is defined as the ratio of accumulated plastic strain to failure strain. The detailed description of the RHT model can refer to LS-DYNA keyword user's manual (Livermore Software, 2020). The accuracy of the RHT model in simulating the dynamic behaviour of rock mass subjected to blast loads has been validated in many previous studies (Huo et al., 2020; Liu et al., 2018; Xie et al., 2017). A total of 38 parameters need to be determined for the RHT model of the rock mass. The basic parameters, such as density, Poisson's ratio, Young's modulus, uniaxial compressive strength, uniaxial shear strength, and uniaxial tensile strength, are obtained from the in-situ geological investigation of the arched Qidaoliang tunnel (Yang, 2006). The failure surface parameters A and N for the strength model, the initial crush pressure, the strain rate dependence exponents β_c (compressive) and β_t (tensile), and the Hugoniot polynomial coefficients A_1, A_2, and A_3 for the equation of state (EOS) are calculated by using the empirical equations in Liu et al. (2018). The remaining parameters are integrated from Liu et al. (2018), Xie et al. (2017), and Huo et al. (2020). **Table 2** lists the parameters of RHT model for rock mass used in this study.

Table 2. RHT model parameters for rock mass (Huo et al., 2020; Liu et al., 2018; Xie et al., 2017; Yang, 2006).

Type of parameter	Specific parameter	Value	Specific parameter	Value
Basic parameters	Density (kg/m^3)	2600	Relative shear strength	0.8
	Compressive strength (MPa)	41	Relative tensile strength	0.08
	Elastic shear modulus (GPa)	28		

Strain rate parameters	Reference compressive strain rate E_{0c}	3e^{-5}	Reference tensile strain rate E_{0t}	3e^{-6}
	Break compressive strain rate E_c	3e^{25}	Break tensile strain rate E_t	3e^{25}
	Compressive strain rate dependence exponent β_c	0.028	Tensile strain rate dependence exponent β_t	0.033
Strength parameters	Failure surface parameter A	2.7	Failure surface parameter N	0.65
	Lode angle dependence factor Q_0	0.68	Lode angle dependence factor B	0.05
	Compressive yield surface parameter G_c	0.53	Tensile yield surface parameter G_t	0.7
	Volumetric plastic strain fraction in tension P_{tf}	0.001	Erosion plastic strain E_{psf}	2
	Shear modulus reduction factor X_i	0.5	Minimum damaged residual strain E_{pm}	0.015
	Residual surface parameter A_f	0.25	Residual surface parameter N_f	0.62
Damage parameters	Damage parameter D_1	0.04	Damage parameter D_2	1
EOS parameters	Initial porosity α_0	1.0	Porosity exponent N_p	3
	Crush pressure P_{el} (MPa)	27.33	Compaction pressure P_{co} (GPa)	6
	Gruneisen gamma γ	0	Hugoniot polynomial coefficient A_1 (GPa)	25.36
	Hugoniot polynomial coefficient A_2 (GPa)	37.34	Hugoniot polynomial coefficient A_3 (GPa)	21
	Parameter for polynomial EOS B_0	1.22	Parameter for polynomial EOS B_1	1.22
	Parameter for polynomial EOS T_1 (GPa)	36.22	Parameter for polynomial EOS T_2	0

2.4 Model calibration

Results of the RC slab subjected to a TNT explosion (Wang et al., 2012) is used to calibrate the lining model and the test of tunnel-like rock chamber subjected to an internal TNT explosion (Wu et al., 2003; Wu et al., 2004; Zhou and Jenssen, 2009) is used to calibrate the model of rock mass. The details are given below.

2.4.1 Lining model calibration

Currently, there is no test data available in the open literature on tunnel lining subjected to internal blast loading. The explosion tests of reinforced concrete (RC) slabs have been widely used in previous studies (Goel et al. (2020); Yang et al. (2019); Zaid and Sadique (2020);) for model calibration and the response prediction of tunnel linings subjected to blast loads . In this study, the calibrated model for the RC slab is also used to predict structural response of tunnel linings due to similar structural configurations and material models of RC slabs and RC lining.

In this study, an experiment of RC slab subjected to a TNT explosion (Wang et al., 2012) is used to calibrate the numerical model for tunnel lining structure. As shown in **Figure 4**(a), the concrete slab with the size of 750 mm and the thickness of 30 mm reinforced by 6mm-diameter steel rebars with the spacing of 75 mm and a reinforcement ratio of 1.43% was subjected to blast loading and results were reported in Wang et al. (2012). The RC slab was firmly clamped on two sides by a steel frame fixed on the ground (see **Figure 4**(b)). A TNT charge of 0.13 kg was detonated at a standoff distance of 0.3 m above the RC slab. The compressive strength of the concrete was 39.5 MPa and the yield strength of steel rebar was 600 MPa. The numerical model is built as shown in **Figure 4**(c). The RC slab is constrained on two sides by steel plates. The keyword *CONTACT_AUTOMATIC_SURFACE_TO_SURFACE is used to simulate the contacts between the fixed steel plates and the concrete slab. The keyword *LOAD_BLAST_ENHANCED is employed to simulate the blast loads from 0.13 kg TNT explosion at a distance of 0.3m from the upper surface of the concrete slab. The mesh sizes of 5 mm and 2.5 mm are respectively selected for concrete and steel rebar elements after conducting mesh convergence tests.

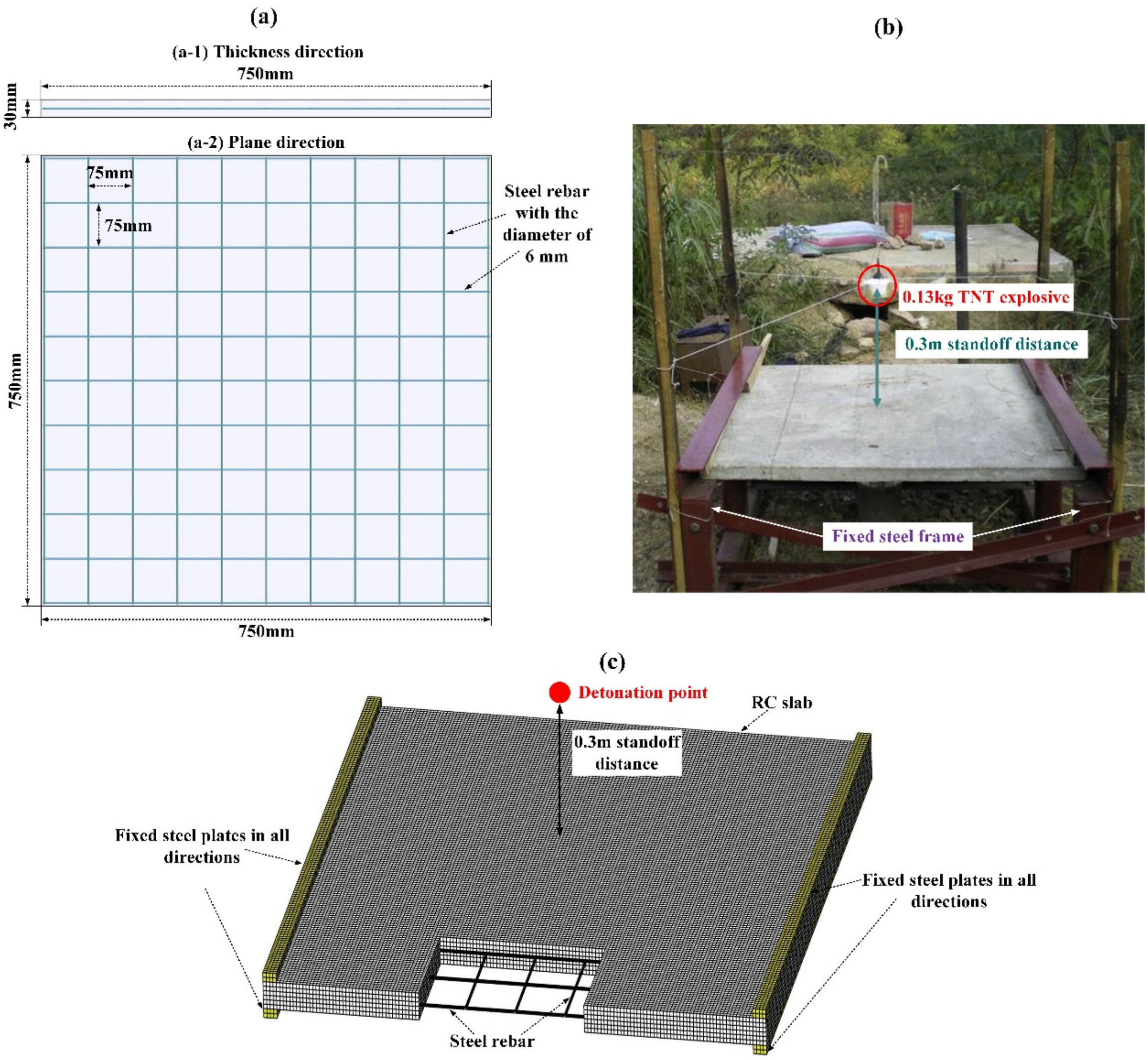

Figure 4. Test setup and numerical model of the RC slab subjected to TNT explosion, (a) geometric configuration of the RC slab, (b) experiment settings (Wang et al., 2012), (c) numerical model.

Figure 5 compares the damage modes of the RC slab observed in the test and simulated by the numerical model. The damage levels of concrete in the numerical simulation are characterized by the effective plastic strain. It can be seen that the concrete damage on the front face of the RC slab predicted by the numerical model agrees well with the distribution of concrete cracks in the test. The damage area on the rear face of the RC slab in the numerical result is also similar to that in the test. The mid-span displacement time history in the numerical model is shown in **Figure 6**. Since the displacement time history of the RC slab in the test was not recorded, only residual displacements of the RC slab from the numerical model and the test are compared. The predicted mid-span residual displacement is 8.25 mm, which is close to 9 mm in the test. It should be noted that more parameter comparisons would definitely give a more confident numerical model. However, only damage modes and displacements are captured from the tests and thus compared with numerical results. Nevertheless, the agreement between the numerical and experimental results demonstrates the accuracy of the lining models, which can be used for the subsequent analysis of lining structure.

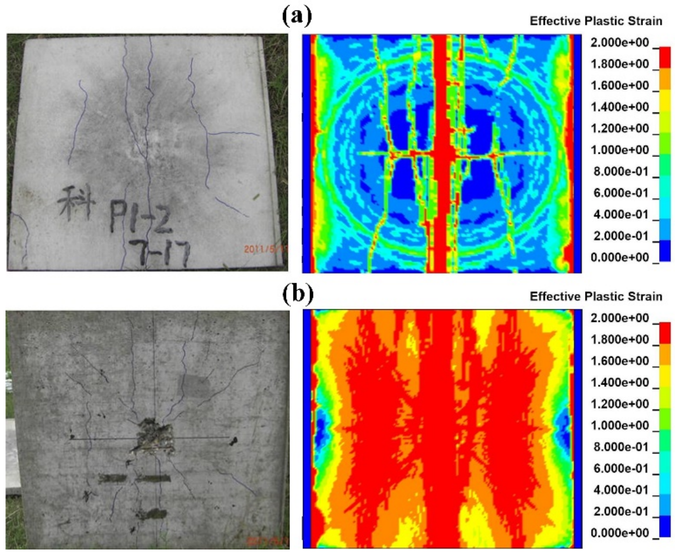

Figure 5. Comparisons of damage modes obtained in the test (Wang et al., 2012) and simulation, (a) the front face, and (b) the back face of the RC slab.

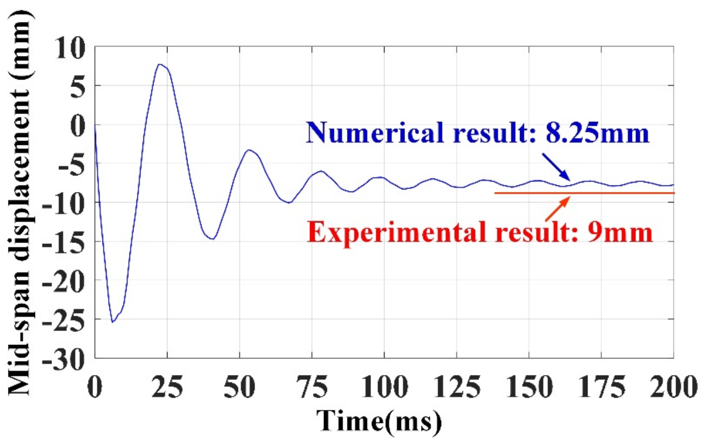

Figure 6. Comparison of mid-span residual displacements obtained in the test (Wang et al., 2012) and the numerical simulation.

2.4.2 Calibration of rock mass model

The rock mass model is calibrated by the field test of an internal explosion on a large-scale underground rock chamber with a cover depth of 80 m, which was carried out in Alvdalen, Sweden in 2001 (Wu et al., 2003; Wu et al., 2004; Zhou and Jenssen, 2009). The tunnel-like rock chamber with the length of 33 m, the width of 8.8 m, and the height of 3.9 m was subjected to an internal explosion of 10 tons of TNT equally divided and placed in two rows inside the chamber with the spacing of 3.4 m in the same cross-section (see **Figure 7**(a)). The spacing between two adjacent charges along the length of chamber was 7.5 m and the spacing between the side charge and the chamber wall was 1.5 m. The centres of ten charges were arranged at the same level of 0.9 m from the floor of the chamber. Three speedometers at the same level (i.e., 1.5 m from the floor of the chamber) were placed at 6 m, 10 m, and 18 m from the right chamber wall, respectively. One pressure gauge is installed on the right wall of the chamber 0.9 m above the floor to measure explosion pressure. The basic mechanical parameters of the rock mass in the numerical model, including the uniaxial compressive strength of 200 MPa, tensile strength of 11 MPa, Young's modulus of 75 GPa, Poisson's ratio of 0.27, and density of 2620 kg/m^3 were obtained by rock mechanical tests (Wu et al., 2003). The remaining parameters are obtained by empirical equations and relevant references, as discussed in Section 2.3.2.

A quarter of the rock chamber and the charge in the test are built in the numerical model. The whole size of the numerical model is 25 m (width) × 36 m (height) × 30 m (length), as shown in **Figure 7**(b). The symmetric boundaries are applied on the front and left surfaces, and non-reflection boundary is assigned for other four surfaces, i.e., back, right, top, and bottom surfaces. Meanwhile, the fixed boundary condition is assigned to the bottom surface to prevent the whole model from moving along *y* direction (i.e., vertical direction). The multi-material ALE method is adopted for the explosive and air by using the keyword *ALE_MULTI-MATERIAL_GROUP, and the rock mass is modelled by Lagrangian mesh. The explosive and air, as well as the air and rock mass, share common nodes at their interfaces. The mesh size of 100 mm is determined for the explosive, air and rock mass around the chamber by conducting mesh convergence test. In the previous studies (Liu et al., 2019; Shi et al., 2008; Wang et al., 2016; Wang and Zhang, 2014; Yang et al., 2019), the 100 mm mesh size was also employed for explosive and air to predict structural response with sufficient accuracy and hence it is adopted in this study. In order to save the computational cost, the mesh size of rock mass is gradually increased from 100 mm to 500 mm with the increased distance away from the chamber.

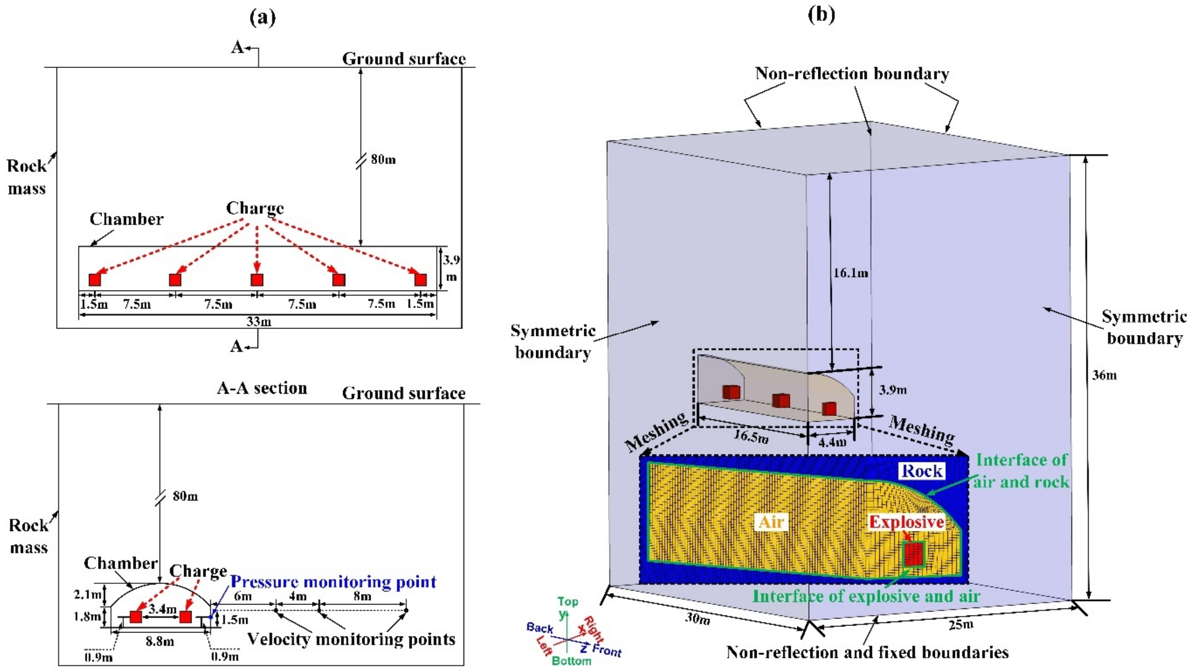

Figure 7. Test setup (Zhou et al., 2002) and numerical model of the underground rock chamber subjected to internal TNT explosions, (a) test setup, (b) numerical model.

Figure 8 compares blast pressure time histories simulated by the CFD model and calculated by the CONWEP method with the measured one at the monitoring point on the chamber wall. It can be seen that the simulated and calculated pressure-time histories agree well with the measured one, which indicates both the CFD explosion model and the CONWEP method can well predict the explosion pressure time history. The equivalent TNT explosion calculated by the CONWEP method instead of the CFD explosive model is used in Section 3.2 to save computational cost.

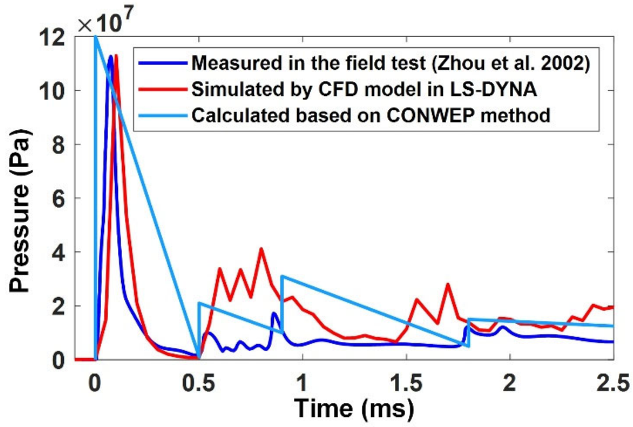

Figure 8. Comparison of measured (Zhou et al., 2002), simulated and calculated (CONWEP) pressure time histories at the pressure monitoring point.

The simulated peak vibration velocities with different scaled distances in rock mass are compared with the test results and their best-fit equation, as shown in **Figure 9**(a). It can be found that the simulated peak vibration velocities have good agreements with the test results and their best-fit curve. The velocity-time histories at 6 m and 10 m from the right chamber wall obtained from numerical simulation and the experimental test are further compared, as shown in **Figure 9**(b). It can be seen that the main waveforms at two locations match well between the simulated and measured results. The simulated waveforms at tails exhibit some smaller oscillations, while no obvious oscillations appear at the tails of the measured waveforms. This is attributed to the effect of site geological discontinuity such as cracks and joints on stress wave absorption, which is not simulated in the numerical model. In addition, the predicted velocity wave arrives earlier than the recorded one in the test at the same location. It might be due to the effect of site geological discontinuity in rock mass on the reduction of average wave velocity, which was not considered in the numerical model. Despite these differences between the numerical and experimental results, the numerical model provides a good prediction for the propagation of stress waves in rock mass with respect to peak particle velocities and velocity waveforms.

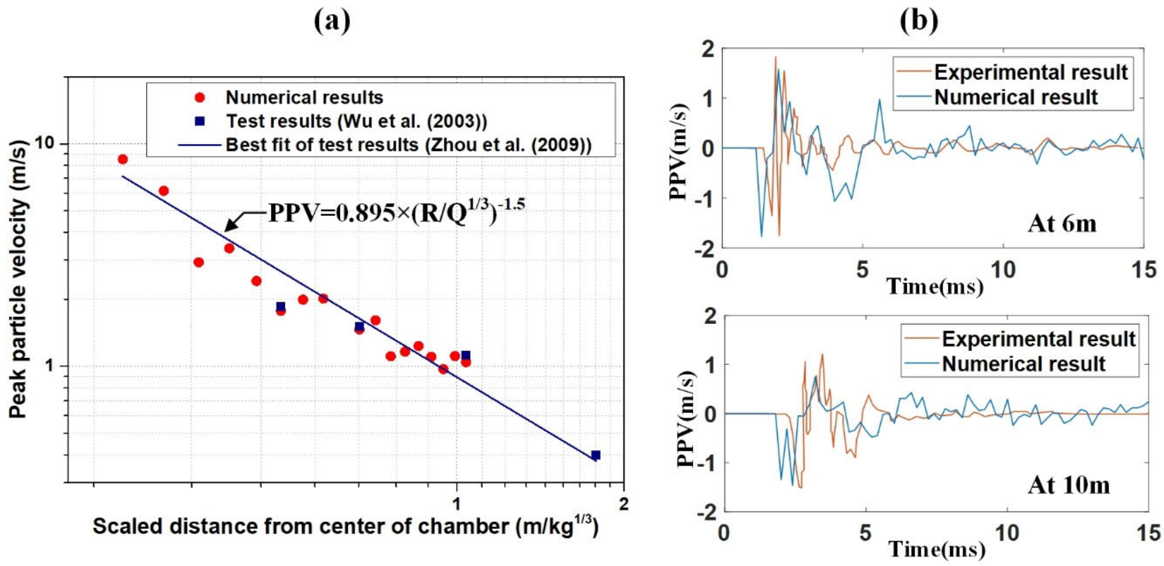

Figure 9. Comparison of (a) peak particle velocities and (b) velocity time histories between the numerical model and the experimental test (Wu et al., 2003; Zhou and Jenssen, 2009).

Zhou et al. (2002) reported that after the internal TNT explosion, ten similar craters on the floor of the rock chamber were formed underneath ten charges, and no obvious rockfall from roof and side walls was observed in the test. In the numerical simulation, ten craters with an approximate diameter of 3 m are also generated on the tunnel floor. **Figure 10**(b) shows five craters (i.e., red plastic strain contours) in the half chamber. It can be found that the numerical result agrees well with the experimental result by comparing the size of a single crater in the field test (see **Figure 10**(a)) with the plastic strain contour from the numerical result (see **Figure 10**(b)). It is also observed that except for severe damage at the corners of tunnel walls in the numerical result, the tunnel walls are predicted suffering only slightly damage, which is consistent with the test result from Zhou et al. (2002).

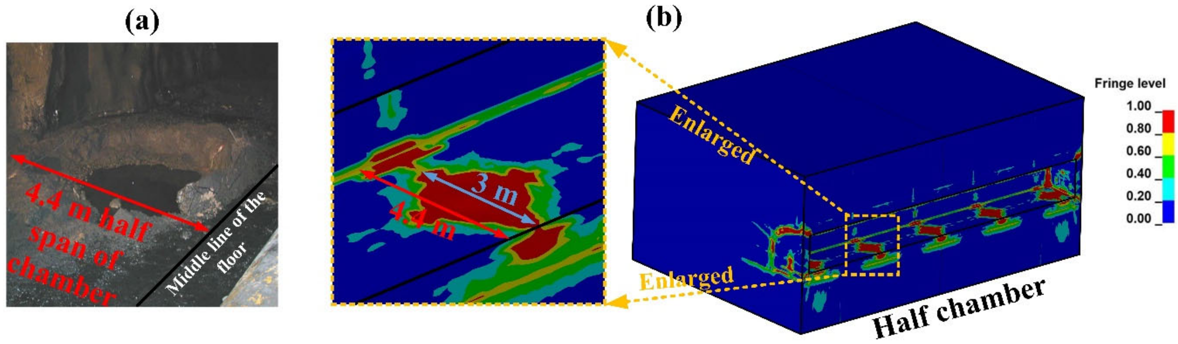

Figure 10. Damage comparisons between (a) experiment (Zhou et al., 2002), and (b) numerical simulation.

3. Road tunnel response to BLEVE and its equivalent TNT explosion load

With the calibrated numerical model, the structural response of the arched tunnel subjected to internal BLEVE is analysed and compared with that subjected to its equivalent TNT explosion load.

3.1 Structural response of tunnel to internal BLEVE

3.1.1 Structural response of composite lining

A total of 38 monitoring points are arranged along the inner surface of the upper arc of arched lining in the cross-section of the BLEVE centre (see **Figure 11**(a)) to investigate the dynamic response of arched lining. The displacements of these monitoring points at different times are shown in **Figure 11**(b). It can be seen that from 0 ms to 7 ms the upper arc of arched lining first experiences uniform radial expansion with the increased BLEVE pressure. The non-uniform radial expansion of the upper arc, i.e., the decreasing displacements from the crown to the springlines (i.e., the junction between the upper arc and lower arc of arched lining) of two haunches, becomes dominant from 7 ms onwards. That is because, with the radial expansion of arched lining, the constraint to the arched lining by the invert is more significant from 7 ms onwards, as shown in **Figure 12**. The apparent non-uniform radial expansion occurs at 11 ms, i.e., the instant of peak displacement, and the residual displacement of the upper arc of arched lining occurs at around 50 ms. It is worth noting that three crests of displacements located at the crown and two shoulders of arched lining are observed at 11 ms. The maximum of peak displacement on the crown of arched lining is caused by the largest sectional moment at this location, as shown in **Figure 13**(a), where 38 monitoring sections of the moment are equally spaced from the two springlines to the crown of arched lining at the cross-section of explosion centre. The crests of displacements at two shoulders are due to large shear forces at the two positions, as shown in **Figure 13**(b), which are caused by the radial expansion of arched lining between the two shoulders and the intensively constrained arched lining between shoulders and springlines.

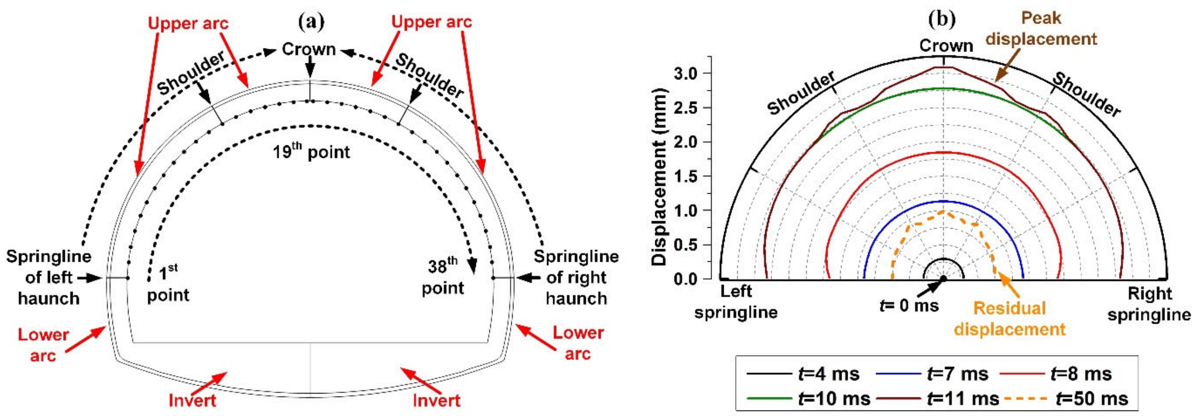

Figure 11. The arrangement of monitoring points along the upper arc of arched lining in the cross-section of the BLEVE centre and corresponding displacement responses, (a) arrangement of monitoring points, (b) displacement responses at different instants.

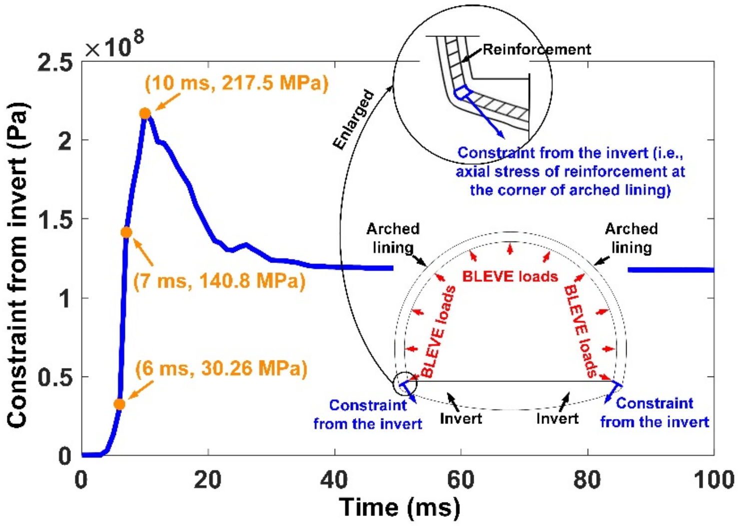

Figure 12. Time history of the constraint to arched lining by the invert (i.e., axial stress of reinforcement at corner).

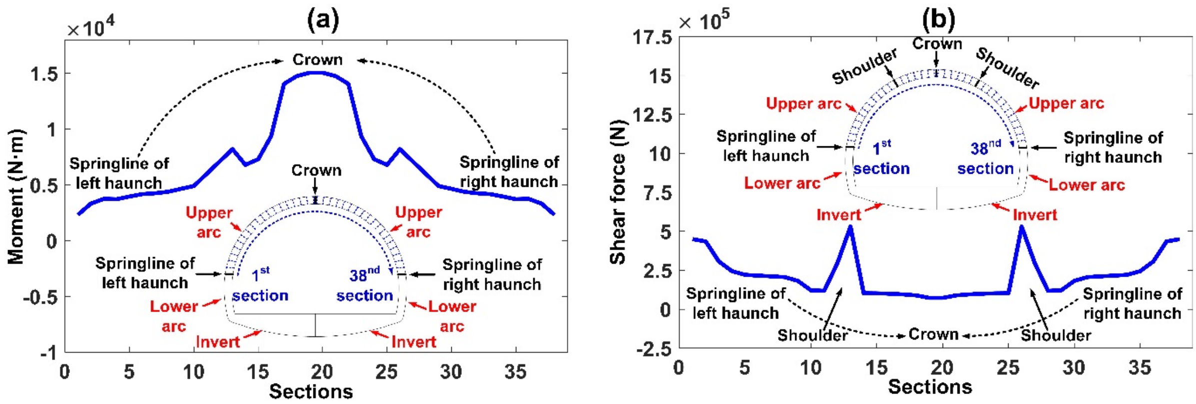

Figure 13. Bending moment and shear force on the upper arc of arched lining at 11 ms, (a) bending moment, (b) shear force.

Figure 14 shows the damage mode of the arched composite lining, including the first and secondary linings subjected to internal BLEVE with the peak pressure of 28 MPa (as given in **Figure 3**). The damage of the arched lining shown in plastic strain contours first occurs at the corner of the arched lining at 4 ms. This is because, with the quickly increased BLEVE pressure, stress concentration occurs at the corner where the geometric shape changes suddenly. Subsequently, the lining damage at the corner extends along the tunnel and the thickness of lining, which is caused by radial expansion of arched lining under internal BLEVE. Meanwhile, the non-uniform radial expansion of arched lining from 8 ms first induces the tensile damage on the inner surface of the upper arc of arched lining near the BLEVE centre due to the larger outward deformation at the upper arc of arched lining. Then the tensile damage on the inner surface of upper arc continues to expand towards two haunches and along the tunnel from 8 ms to 12 ms. At 12 ms, multiple longitudinal cracks on the outer surface of the upper arc of arched lining are generated due to large moments at the upper arc of arched lining (see **Figure 13**(a)). The lining damage is aggravated at the corner and on the inner and outer faces of the upper arc of arched lining from 12 ms to 20 ms. After 20 ms, the damage at the crown and corner continues to increase until passing through the whole lining segment along the tunnel, while the damage at other parts of the upper arc of arched lining is hardly changed.

It can be concluded that the damage of arched lining under internal BLEVE concentrates at two locations: i.e., (1) the corners with the sudden change in geometry and (2) the upper arc of arched lining due to large sectional moments as shown in **Figure 13**(a). In addition, the cross-sectional tensile damage areas on the inner surface of arched lining are gradually reduced with the increased distance along the length of tunnel, which is caused by the decreased BLEVE pressure on the lining.

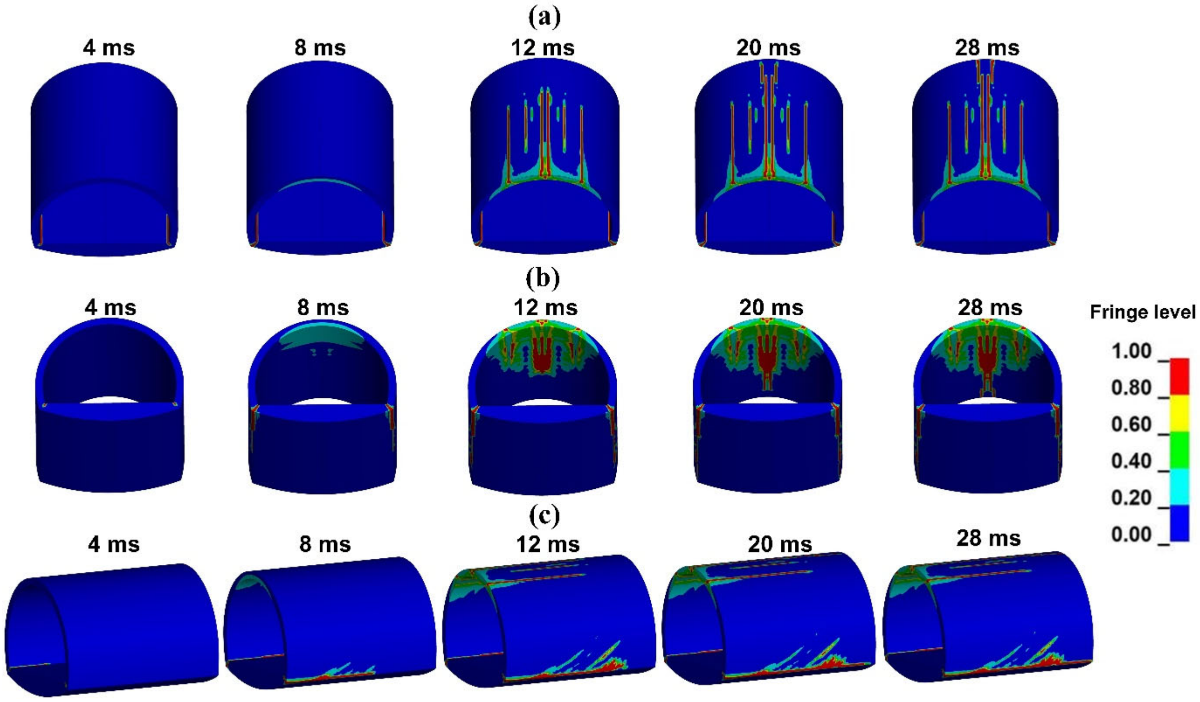

Figure 14. Damage modes of tunnel lining subjected to internal BLEVE, (a) top view, (b) bottom view, and (c) side view.

The damage criterion based on crack grades of concrete developed by Yang et al. (2019) is used to evaluate the damage levels of tunnel lining in this study. **Table 3** lists the crack indexes for four damage levels of lining, i.e., slight damage, moderate damage, severe damage, and collapse. **Figure 14** shows that the penetrating cracks (i.e., cracks running through the thickness of lining) at the corner of arched lining develop through the whole lining segment along the tunnel while penetrating cracks at the crown of arched lining do not develop through the whole lining segment considered in the numerical model. No penetrating crack is presented at other parts of the arched lining. Therefore, it can be concluded that the lining at the corner and crown of tunnel respectively experience severe damage and moderate damage. The remaining part of the upper arched lining experiences slight damage.

Table 3. Damage levels of tunnel lining based on crack grades (Yang et al., 2019)

Damage level	**Damage index**
Slight damage	No penetrating cracks (i.e., no cracks running through the thickness of lining)
Moderate damage	Short penetrating cracks
Severe damage	Penetrating cracks running through the whole lining wall

Collapse	The coalescence of multiple penetrating cracks running through the whole lining wall

3.1.2 Structural response of rock surroundings

Figure 15 presents the damage process of rock surroundings of the arched tunnel subjected to internal BLEVE in the form of the ratio of accumulated plastic strain to failure strain. The damage of rock surroundings first occurs at the corner (e.g., the damage at 8 ms). Then the rock damage at the upper arc of arched tunnel initiates and expands with the increased damage at the corner (e.g., the damage from 12 ms to 50 ms). Thus, it can be concluded that the damage of rock surroundings concentrates at the corner and upper arc of the arched tunnel, which are similar to the damage locations of lining. However, the damage level of rock surroundings is much lower than that of the lining.

A total of 49 monitoring points are equally spaced along the rock surroundings outside the arched lining in the cross-section of the BLEVE centre to obtain the vibration response of rock surroundings, as shown in **Figure 16**(a). **Figure 16**(b) shows peak particle velocities (PPVs) at these monitoring points. It can be seen that the largest PPV occurs at the rock mass around the tunnel crown and reaches 0.82 m/s. Hendron (1977) proposed the damage criterion based on PPV for rock surroundings of tunnel, that is, intermittent failure (i.e., slight damage) with PPV less than 1.8 m/s, local failure (i.e., moderate damage) with the maximum PPV limit of 4 m/s, and general failure (i.e., severe damage) with the maximum PPV limit of 12 m/s. According to these damage criteria, the rock surroundings of the tunnel experience slight damage.

Based on the above analysis, the tunnel lining experiences more severe damage than rock mass surrounding the tunnel under internal BLEVE. More attention should be paid to the response of tunnel lining subjected to internal BLEVE.

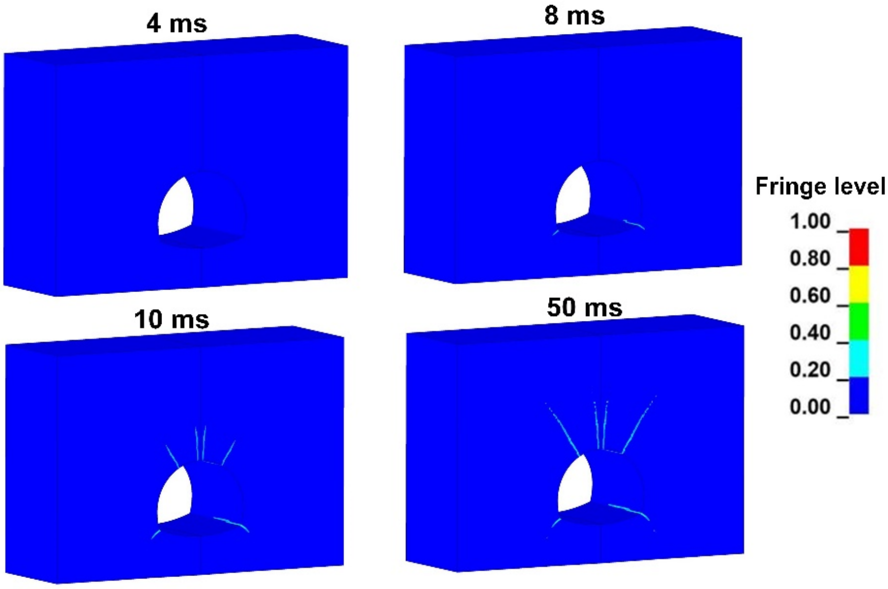

Figure 15. Damage process of rock surroundings of the arched tunnel subjected to internal BLEVE.

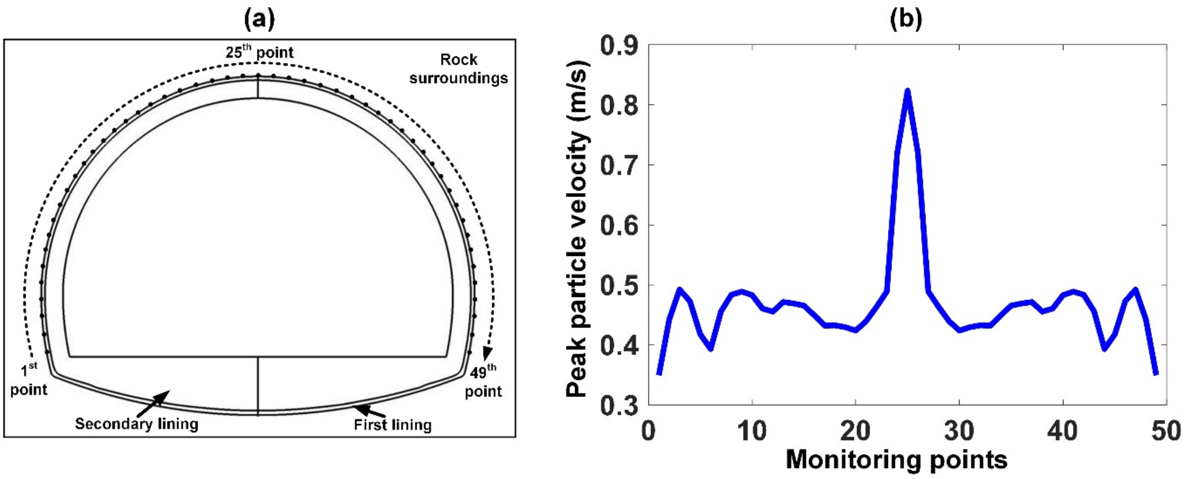

Figure 16. Peak particle velocities along rock surroundings outside the arched lining at the cross-section of the BLEVE centre

3.2 Comparison of tunnel responses subjected to BLEVE and TNT equivalency load

Because of the challenges in predicting BLEVE loads, BLEVE loads are often approximated in analysis and design of structures subjected to BLEVE. Among them, TNT equivalency is a popularly used method to predict BLEVE loads. The TNT equivalence method converts the explosion energy of BLEVE into an equivalent weight of TNT. Therefore, the energy released by BLEVE is used to determine the equivalent weight of TNT and the subsequent blast loads. Many methodologies based on different thermodynamic and physical assumptions (Hemmatian et al., 2017; Planas-Cuchi et al., 2004; Prugh, 1991) have been developed to calculate the mechanical energy of BLEVE. Hemmatian et al. (2017) compared six common methods of calculating BLEVE energy. Although the method proposed by Prugh (1991) is slightly conservative, the remaining methods inaccurately estimate the mechanical energy release to a larger extent. For instance, the worst-case scenarios (e.g., the vapour expansion with the flashing of 80% liquid in the LPG tanker) were arbitrarily assumed in those methods. Therefore, the method proposed by Prugh (1991) is employed in this study to estimate the equivalent TNT explosion since the energy can be more accurately calculated. The method is expressed below.

$$W_{TNT} = \frac{\left(2.4\times10^{-4} PV^{*}\right)}{k-1}\left(1-\left(101/P\right)^{(k-1)/k}\right) \tag{4}$$

in which

$$V^{*} = V_T + W_L\left(\left(f/D_{V;T}\right)-\left(1/D_{L;T}\right)\right) \tag{5}$$

$$f = 1 - e^{\left(-\Omega\frac{C}{L}(T_c - T_b)\right)} \tag{6}$$

$$\Omega = 2.63\left(1-\left(\frac{T_c - T_0}{T_c - T_b}\right)^{0.38}\right) \tag{7}$$

where W_{TNT} is the equivalent TNT weight, P is the container pressure, i.e., 50 MPa in this study, V^{*} is the volume of vapour space, k is the specific heat ratio, V_T is the container volume, i.e., 20 m^3 in this study, W_L is the weight of liquid in the container, f is the flashing fraction; $D_{V;T}$ and $D_{L;T}$ are the density of the liquid and saturated vapour in the container, respectively; T_c, T_0, and T_b are the critical temperature, the initial temperature, and the boiling point of LPG, respectively; C and L are the average specific heat of compressed liquid and the average latent heat of vaporization, respectively. Based on the critical pressure P and critical temperature T_c of the LPG container, the parameters mentioned above are obtained from the NIST fluid properties reference Version 8.0 (Lemmon et al., 2007), and the equivalent TNT weight of the BLEVE is calculated as listed in **Table 4**.

Table 4. Parameters for the calculation of TNT equivalence of BLEVE

T_c (k)	P (kPa)	T_b (k)	T_0 (k)	C (kJ/kg/k)	L (kJ/kg)	$D_{L;T}$ (kg/m^3)	$D_{V;T}$ (kg/m^3)	V_T (m^3)	W_L (kg)	k	W_{TNT} (kg)
370.15	50000	231.15	288.15	2.43	427	511.92	57.681	20	7680	1.4081	1146

The blast loading profiles of the equivalent TNT (i.e., the arrival time, the duration, and peak reflected pressure) applied on the first 8m tunnel wall along the tunnel are calculated by the conventional weapons effects program (CONWEP) in UFC 3-340-02 (US Department of Defense, 2008) based on the equivalent TNT weight and the detonation distance, in which the first 8 m tunnel wall is divided into 8 segments with 1m interval along the tunnel, as described above in calculating the BLEVE loads. The calculated TNT loading profiles (as shown in **Figure 17**) are applied onto 8 segments of tunnel, respectively. It should be noted that TNT explosion loads are applied to the arched lining as the case of BLEVE loads.

Figure 18 shows the pressure-time histories of BLEVE and its equivalent TNT explosion load applied onto the first segment. Compared to BLEVE, the equivalent TNT explosion generates the blast load with higher peak pressure, shorter rising time, shorter duration and lower impulse. It should be noted that the TNT explosion load applied to the first 1m segment has the highest frequency among all the applied TNT explosion loads on tunnel segments. Majority of the blast loading energy is distributed within 1500 Hz. Since the wave velocities of concrete and rock mass are no less than 2200 m/s, the allowable maximum mesh size should be 122 mm or less under the TNT explosion loading. The mesh size of 100 mm around the tunnel is smaller than the allowable mesh size and thus can ensure the accuracy of the model subjected to the TNT explosion loadings.

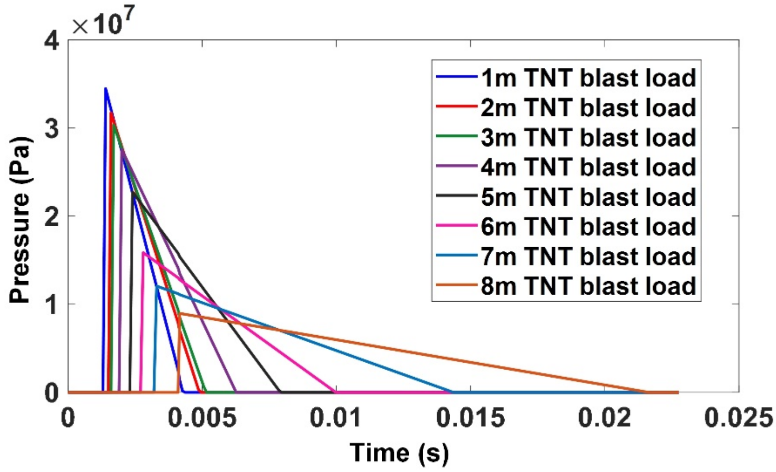

Figure 17. The applied equivalent TNT explosion load on 8 segments of tunnel

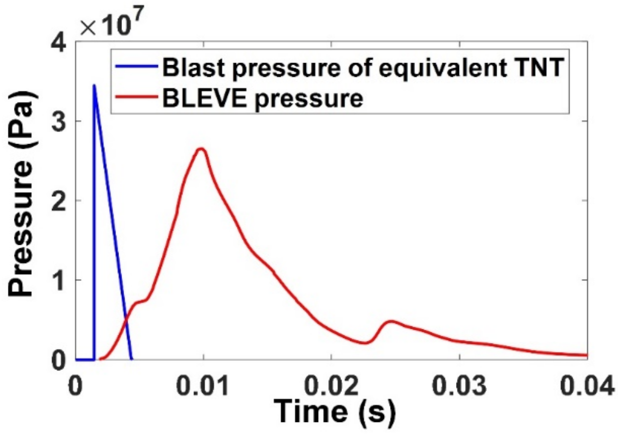

Figure 18. Pressure time histories of BLEVE and equivalent TNT explosion applied onto the first 1 m segment of tunnel.

Figure 19 shows the displacement responses of the upper arc of arched lining at the cross-section of the explosion centre subjected to the equivalent TNT explosion load and BLEVE load at different time instants. As shown in **Figure 19**(b), the upper arc of arched lining subjected to the equivalent TNT explosion load only experiences uniform radial expansion but nearly no non-uniform radial expansion, implying the constraint to the arched lining by the invert is not intensively activated under the TNT equivalent load. This is because, as compared to BLEVE, the TNT equivalent explosion generates blast pressures with shorter rising time (almost instantaneous), which means there is no sufficient time for the invert to activate its intensive constraint, as shown in **Figure 20**. The upper arc of arched lining under equivalent TNT explosion experiences the peak displacement at 3 ms, which is earlier than that under

BLEVE. In addition, the peak displacements of arched lining between two shoulders under equivalent TNT explosion are lower than those under BLEVE at the same monitoring location, which is attributed to the shorter duration and lower impulse of TNT equivalent explosion pressures as compared to BLEVE pressures with the same energy release (see **Figure 18**). However, more intensive constraint to the arched lining by the invert under BLEVE causes smaller displacements of arched lining between shoulders and springlines.

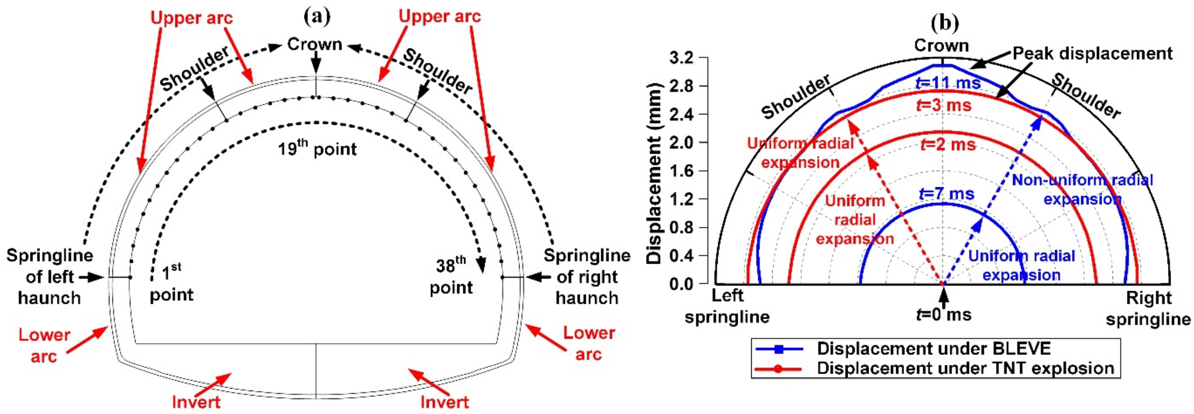

Figure 19. (a) Arrangements of monitoring points, (b) displacement responses at different time instants under BLEVE and equivalent TNT explosion load

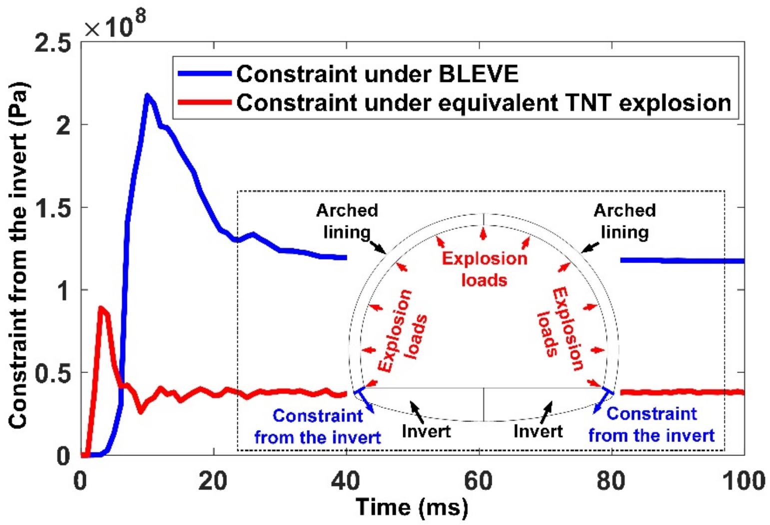

Figure 20. Time histories of constraints to arched lining by the invert under BLEVE and equivalent TNT explosion load

The damage modes of arched lining subjected to the internal equivalent TNT explosion are shown in **Figure 21** in the form of plastic strain contours. It can be seen that under the equivalent TNT explosion, the penetrating damage develops through the whole cross-section of arched lining and over 8m along the length of tunnel, which covers a much larger damage area than that subjected to internal BLEVE (see **Figure 14**). This is because the TNT equivalent explosion with a shorter rising time and higher pressure can induce higher shear stress and hoop tensile stress along the cross-section of arched lining as compared to BLEVE, as shown in **Figure 22**, where 42 areas and 38 sections are divided to obtain peak radial shear stresses and hoop tensile stresses along the cross-section of arched lining at the explosion centre. The shear and tensile stresses along the cross-section of arched lining under TNT explosion both reach the critical shear and tensile strength of lining concrete, i.e., 1.9 MPa and 1.96 MPa with compressive and tensile strain rates of 1 s^{-1} and 0.1 s^{-1} (Bresler and Pister, 1958; Ministry of Transport of the People's Republic of China, 2018; US Department of Defense, 2008). According to the damage criterion based on crack grades, the damage of the arched lining subjected to the equivalent TNT explosion load is rated as collapse-level. **Figure 23** shows the time histories of strain energy of arched lining subjected to BLEVE and its equivalent TNT explosion. It can be seen that peak and residual strain energies of arched lining subjected to the TNT equivalent explosion load are 83.4% and 380% higher than those subjected to the BLEVE, respectively. Therefore, with the same explosion energy, it can be concluded that the structural damage of tunnel lining subjected to BLEVE is significantly less severe than that subjected to the equivalent TNT explosion load.

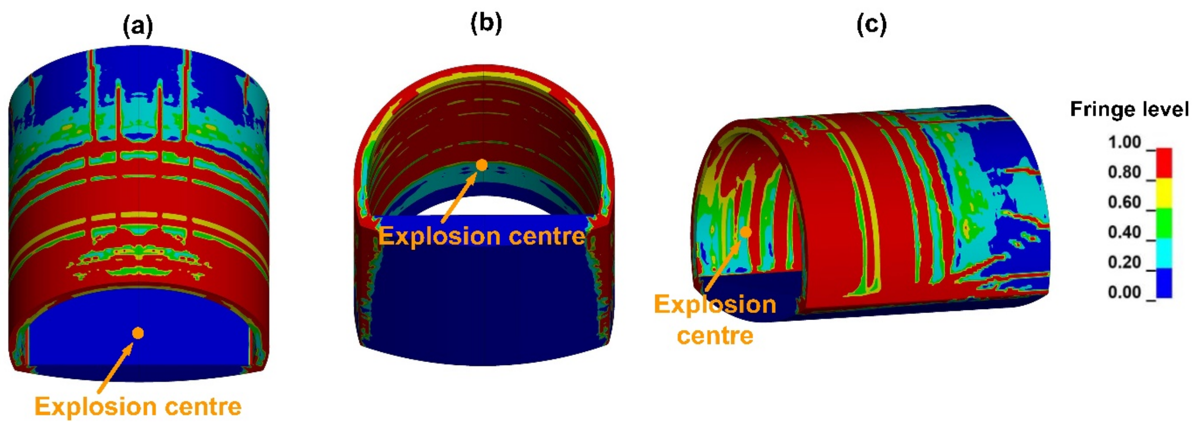

Figure 21. Damage modes of the lining subjected to the equivalent TNT explosion load, (a) top view, (b) bottom view, and (c) side view.

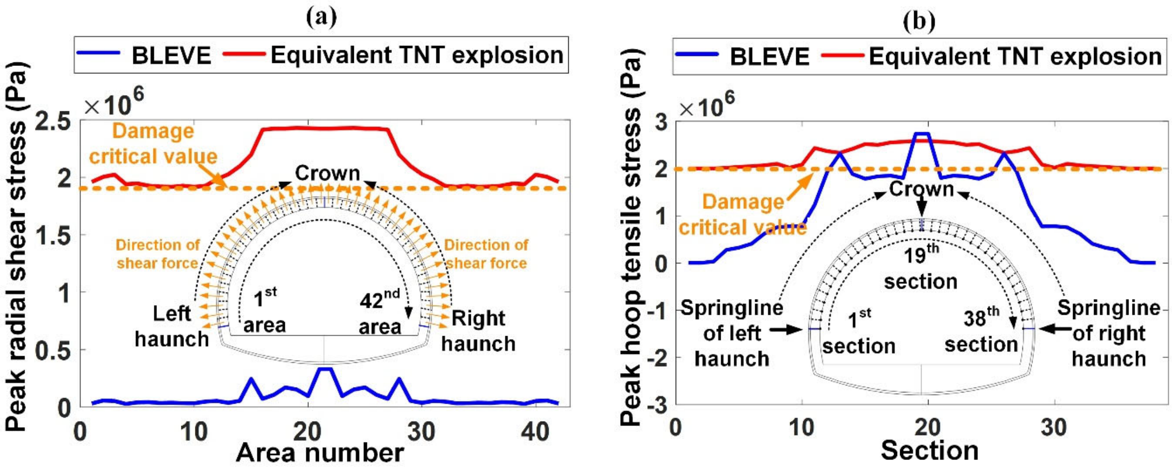

Figure 22. Peak radial shear stress and hoop tensile stress along the arched lining at the cross-section of explosion centre, (a) peak radial shear stress, (b) peak hoop tensile stress.

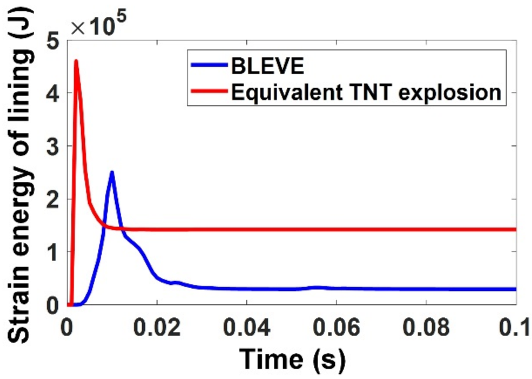

Figure 23. Time histories of strain energy of arched lining subjected to BLEVE and its equivalent TNT explosion load

4. Parametric study

Dynamic response of the arched tunnel subjected to BLEVE and its equivalent TNT explosion load has been investigated in section 3. The results indicate that using the empirical method (i.e. the TNT equivalency explosion method by Prugh (1991)) to predict BLEVE overpressures would lead to significant overestimation of structural damage. Therefore, BLEVE overpressures obtained from FLACS simulations are utilized in the subsequent analysis. Parametric studies are further conducted to investigate the influences of concrete grade, concrete thickness, steel reinforcement ratio, and surrounding stiffness on the dynamic response of tunnel lining subjected to internal BLEVE. The factors of tunnel lining considered in this study include concrete grades, concrete thicknesses, and reinforcement ratios. The values are chosen according to the Chinese design code of road tunnel JTG 3370.1-2018 (Ministry of Transport of the People's Republic of China, 2018).

4.1 Effect of concrete grades

Four grades of concrete C15, C25, C35 and C45 (i.e., concretes with the compressive strengths of 15 MPa, 25 MPa, 35 MPa and 45 MPa) are considered with other parameters unchanged in this section to investigate the effects of concrete grades of lining on the dynamic response of the arched tunnel. **Figure 24** shows the damage modes of the arched lining with different concrete grades. As shown, the damage on the inner and outer surface of the upper arc of arched lining is gradually decreased with the increased concrete grades due to the increased tensile strengths of concrete. Two penetrating tensile cracks (i.e., cracks running through the thickness of lining) develop through the upper arc of the whole lining segment along the tunnel with C15 grade of concrete, and tensile cracks do not always penetrate the thickness of upper arc of the whole lining segment along the tunnel with higher grades of concrete as circled in **Figure 24**. In comparison, the arched lining with C15 grade of concrete experiences severe damage, while the arched linings with higher grades of concrete experience moderate-to-slight damage. The time histories of average strain energy (i.e., strain energy divided by the thickness of arched lining) of arched lining with different concrete grades are presented in **Figure 25**. Peak average strain energy of arched lining decreases by 22.7% from C15 concrete to C45 concrete.

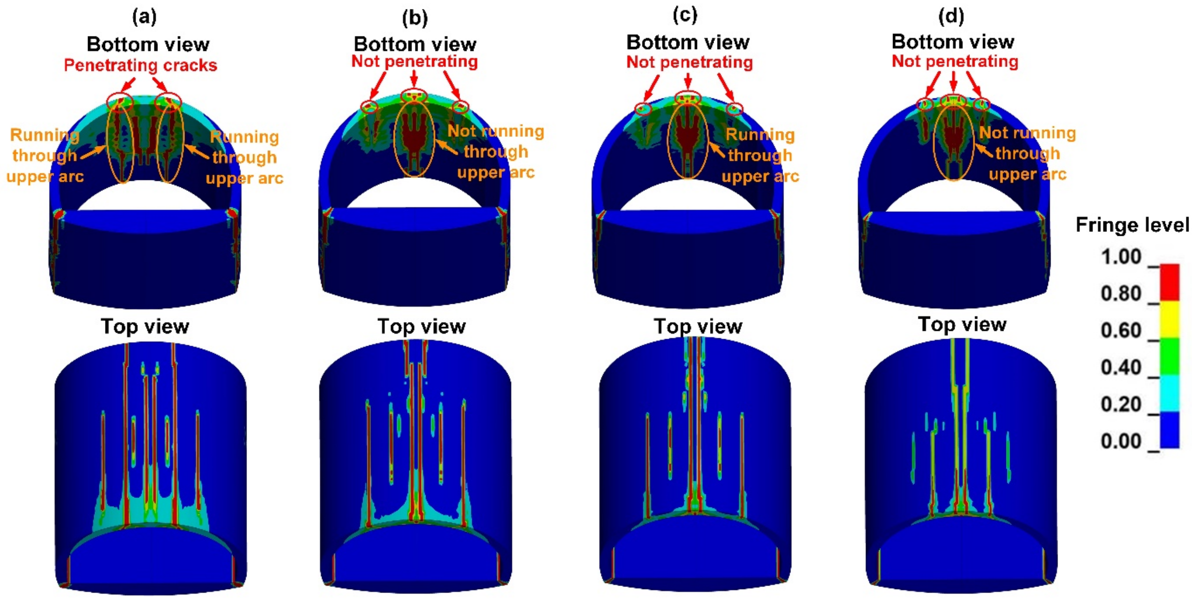

Figure 24. Damage modes of the arched lining with (a) C15 concrete, (b) C25 concrete, (c) C35 concrete, and (d) C45 concrete subjected to the same internal BLEVE.

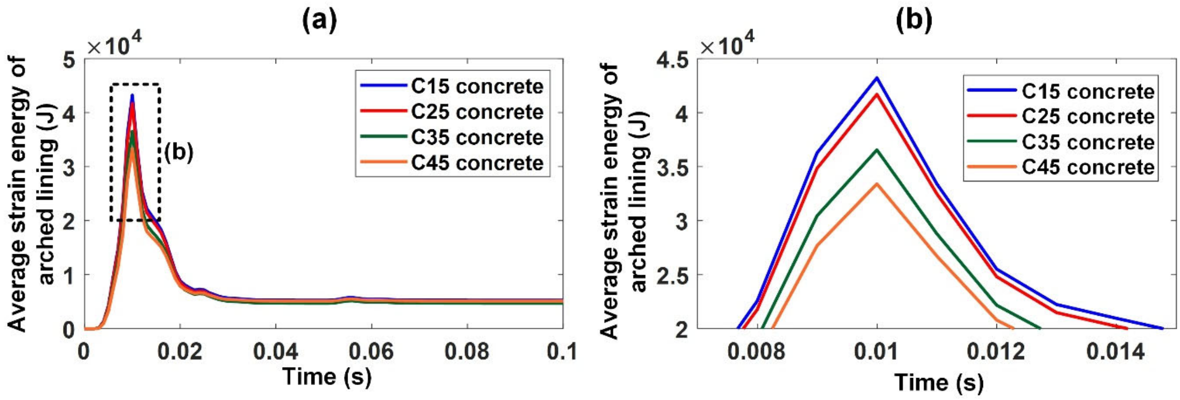

Figure 25. Average strain energy time histories of arched lining with different concrete grades, (a) full time histories of average strain energy, (b) enlarged

4.2 Effect of concrete thickness

The composite linings with the thicknesses of 500 mm, 600 mm, 700 mm and 800 mm are considered in this section to investigate the effect of lining thickness on the dynamic response of arched tunnel subjected to BLEVE. The damage modes of arched lining with four concrete thicknesses against the same internal BLEVE are presented in **Figure 26**. The damage areas on the inner and outer surfaces of the upper arc of arched lining gradually decrease with the increased concrete thickness. This is because increasing concrete thickness enhances the sectional stiffness of concrete and thus decreases the levels of tensile strains on the lining. Penetrating cracks develop through the upper arc of the whole lining segment along the tunnel lining with a thickness of 500 mm. However, cracks do not always penetrate the thickness of upper arc of the whole lining segment along the tunnel with the lining thickness over 500 mm. **Figure 27** shows the time histories of average strain energy of arched lining with different concrete thicknesses. Peak average strain energy decreases by 16.2% with the increasing thickness of concrete from 500 mm to 800 mm.

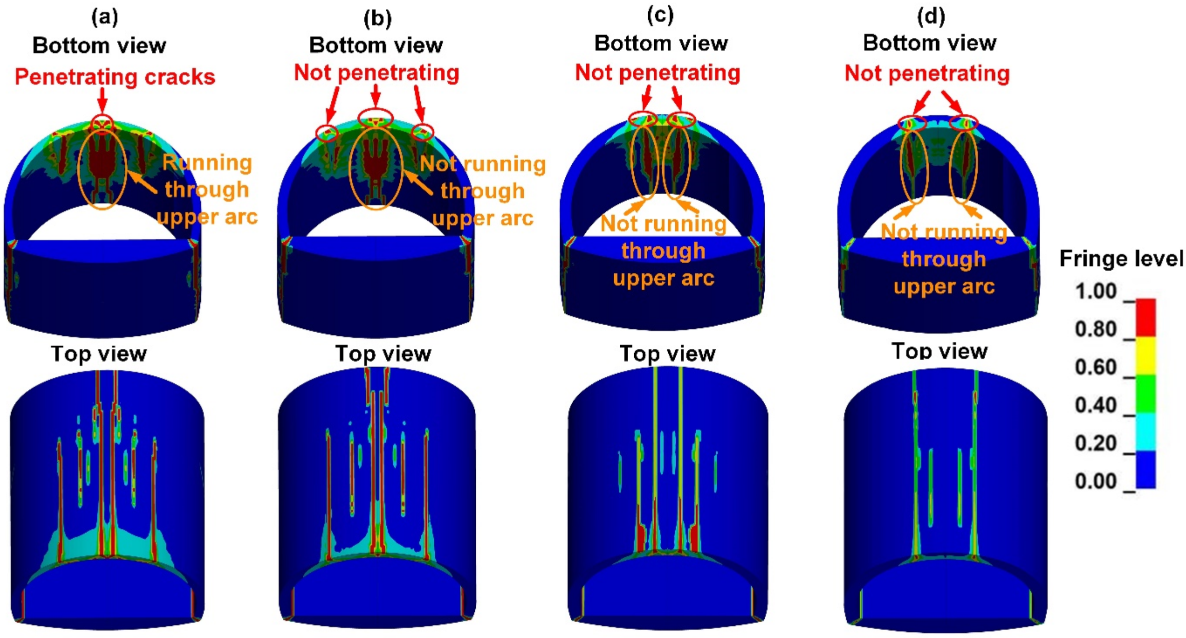

Figure 26. Damage modes of the arched composite lining with the thickness of (a) 500 mm, (b) 600 mm, (c) 700 mm, and (d) 800 mm subjected to the same internal BLEVE.

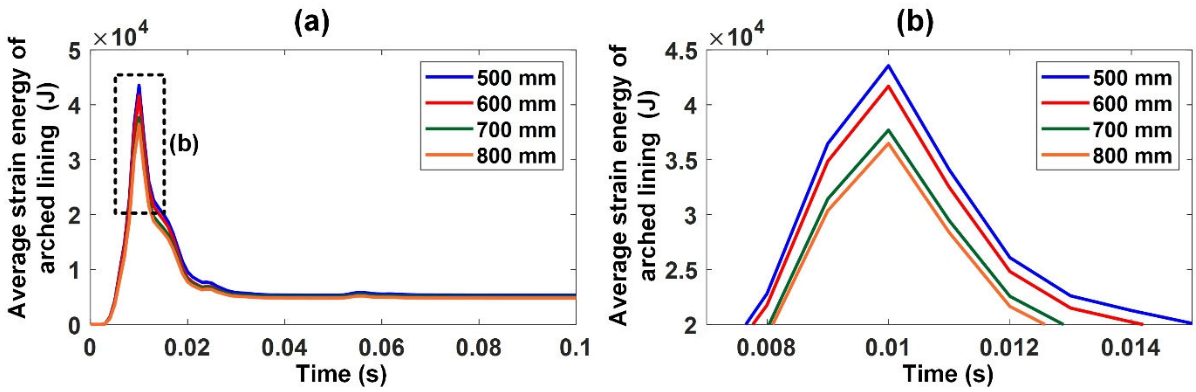

Figure 27 Average strain energy time histories of arched lining with different concrete thicknesses, (a) full time histories of average strain energy, (b) enlarged.

4.3 Effect of steel reinforcement ratios

Four reinforcement ratios of 0.63%, 1.41%, 2.51%, and 3.92% for hoop and longitudinal reinforcements in the secondary lining are modelled by changing the diameter of reinforcements as 20 mm, 30 mm, 40 mm, and 50 mm, respectively to investigate the effects of reinforcement ratios on the BLEVE-resistant performance of tunnel lining. **Figure 28** presents the damage modes of lining with different reinforcement ratios against the same internal BLEVE load. It can be seen that increasing reinforcement ratios only decreases the damage on the distal inner and outer surfaces of the upper arc of arched lining along the tunnel, while the damage on other parts of arched lining is not obviously changed with varying reinforcement ratios. The results illustrate that with the restraint of rock surroundings to the deformation of lining, the influence of changing steel reinforcement ratios on the bending damage of lining subjected to internal BLEVE loading is not prominent. It is observed that the damage areas around the corner of lining are gradually increased with the increased reinforcement ratios, which may be attributed to that the concentrated stresses at the corner transferred towards the surrounding concrete. The time histories of average strain energy of arched lining with four reinforcement ratios are shown in **Figure 29**. The peak average strain energy of arched lining only decreases by 8% with the reinforcement ratios increased from 0.63% to 3.92%.

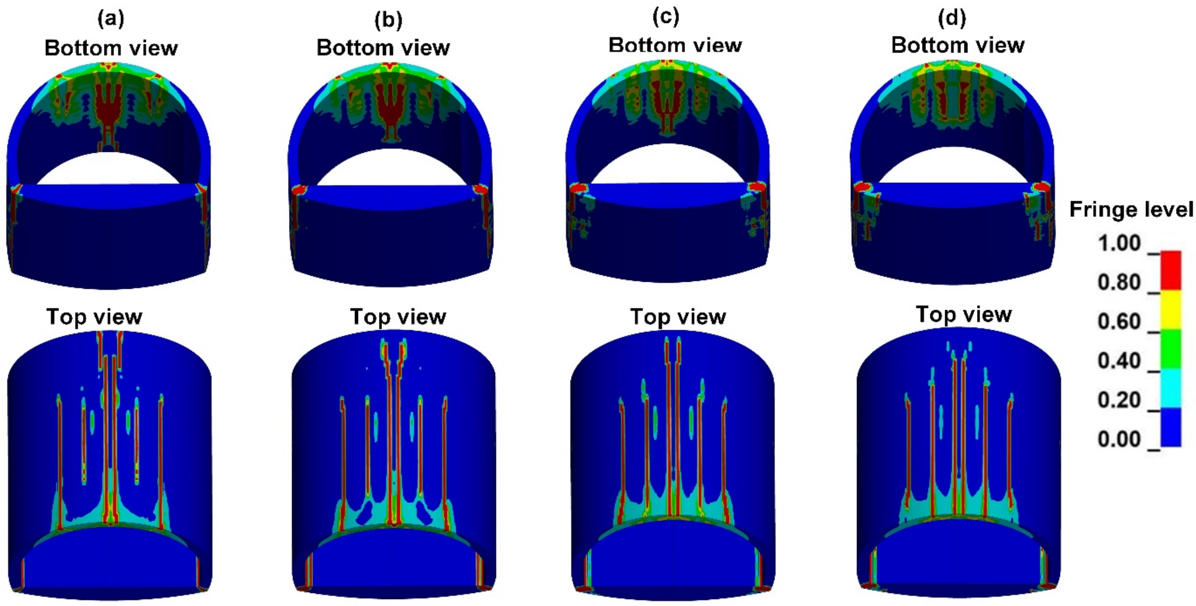

Figure 28. The damage modes of the arched lining with the reinforcement ratios of (a) 0.63%, (b) 1.41%, (c) 2.51%, and (d) 3.92% subjected to the same internal BLEVE.

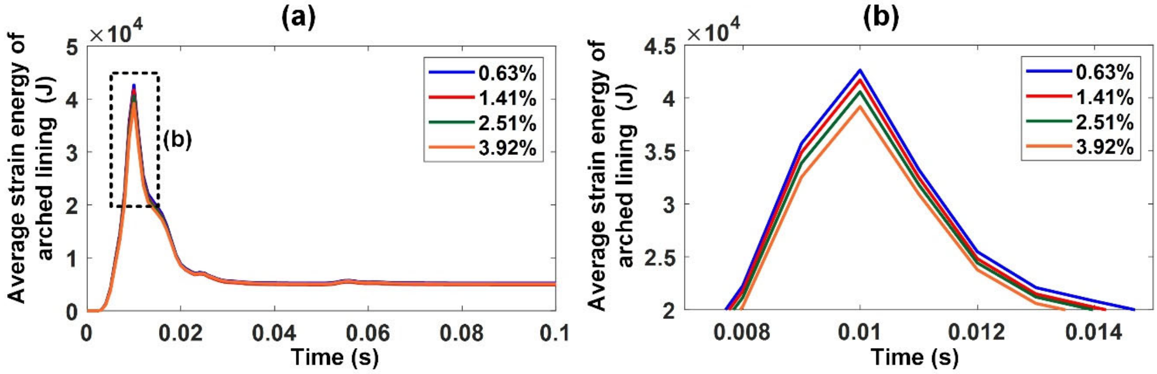

Figure 29. Average strain energy time histories of arched lining with different reinforcement ratios, (a) full time histories of average strain energy, (b) enlarged.

4.4 Effect of surrounding rock mass stiffness

To investigate the effect of stiffness of tunnel surroundings (e.g., due to weathering) on the dynamic response of tunnel lining subjected to internal BLEVE, the rock surroundings with the elastic modulus of 35 GPa, 45 GPa, 55 GPa and 65 GPa (i.e., the corresponding shear modulus of 10.94 GPa, 19.40 GPa, 23.71 GPa, and 28.01 GPa with Poisson's ratio of 0.16 (Yang, 2006)) are considered in this section. The damage modes of arched lining surrounded by four types of rock masses against the same internal BLEVE are shown in **Figure 30**. It can be seen that the damaged areas on the inner and outer surfaces of arched lining significantly decrease with the increased surrounding stiffness. The results indicate that surrounding rock mass with higher stiffness leads to smaller deformation of the arched lining. With the rock stiffness of 35 GPa and 45 GPa, penetrating cracks are observed through the upper arc of the whole lining segment along the tunnel segment. With the rock stiffness of 55 GPa and 65 GPa, cracks do not always penetrate the thickness of upper arc of the whole lining segment along the tunnel segment. That is to say, the arched lining with rock stiffness less than or equal to 45 GPa and over 45 GPa respectively experiences severe damage and moderate-to-slight damage. In addition, the time histories of average strain energy of arched lining surrounded by the rock mass with four kinds of surrounding rock mass stiffness are shown in **Figure 31**. As shown, the peak and residual average strain energies of arched lining respectively decrease by 13% and 52.9%, when the elastic modulus increases from 35 GPa to 65 GPa.

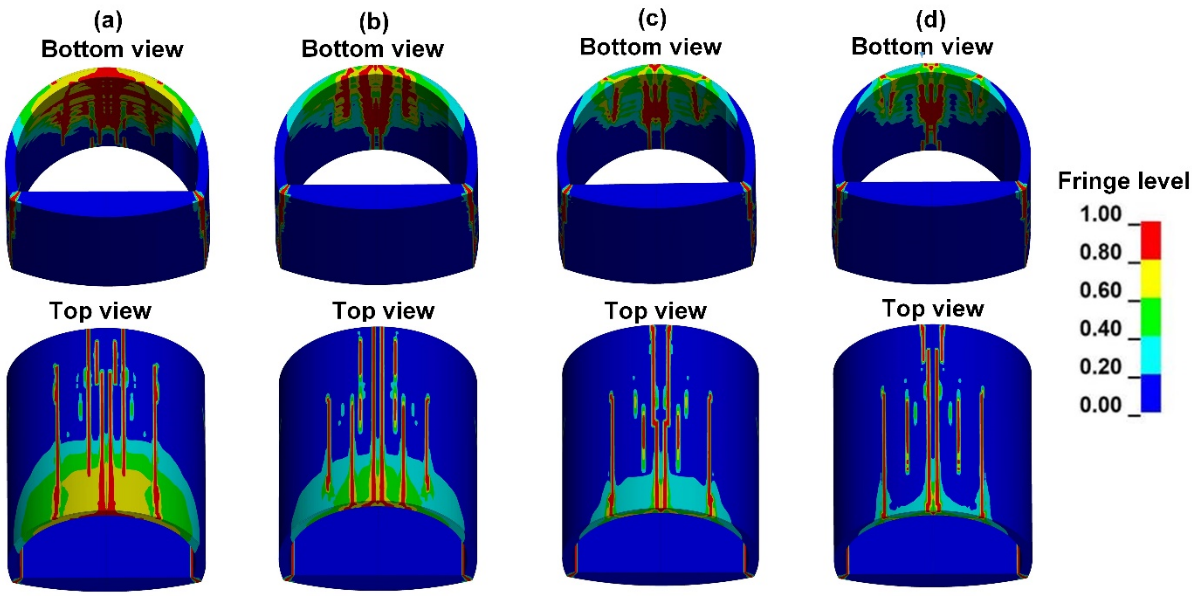

Figure 30. Damage modes of the arched lining surrounded by rock with elastic modulus of (a) 35 GPa, (b) 45 GPa, (c) 55 GPa, and (d) 65 GPa subjected to the same internal BLEVE

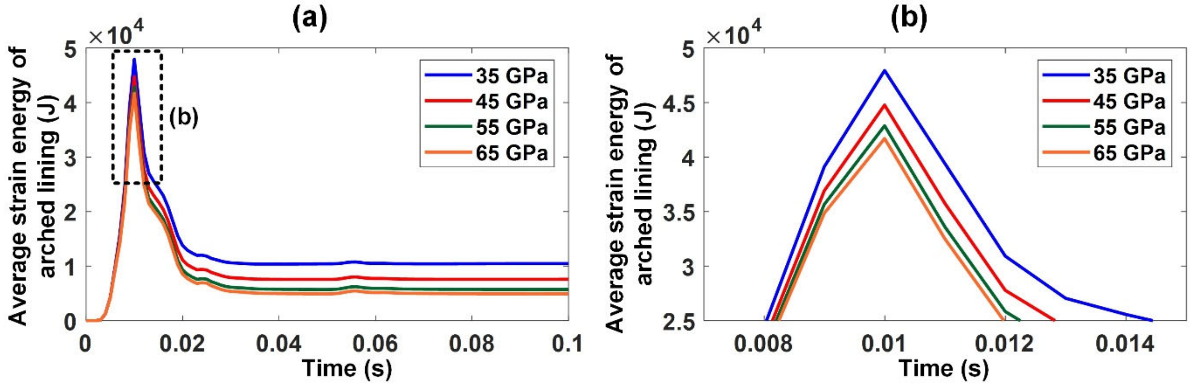

Figure 31. Average strain energy time histories of arched lining surrounded by the rock with different elastic modulus, (a) full time histories of average strain energy, (b) enlarged.

5. Concluding remarks

In this study, dynamic response of arched tunnels subjected to internal BLEVE has been numerically investigated by using LS-DYNA. The numerical models of lining and rock surroundings subjected to blast loading are calibrated by using the existing tests of an RC slab and a tunnel-like rock chamber subjected to TNT explosions, respectively. Good agreements between the numerical and experimental results are obtained in terms of the damage mode and mid-span displacement of the RC slab as well as the damage mode and vibration velocity of the rock mass. With the calibrated numerical model, dynamic responses of the arched tunnel subjected to internal BLEVE are investigated and compared with those subjected to its equivalent TNT explosion load. Parametric studies are also conducted to investigate the effects of concrete grade, concrete thickness, steel reinforcement ratio, and surrounding rock mass stiffness on the dynamic response and damage modes of tunnel subjected to internal BLEVE. Based on the numerical results, the following conclusions can be drawn:

(1) Severe damage of arched tunnel subjected to the considered internal BLEVE is presented at the corner of lining because of stress concentration due to the sudden change in geometry, as well as at the upper arc of arched lining due to the large bending moment at the upper arc of arched lining. Rock surroundings experience only slight damage. Therefore,

protective measures are suggested for the corner and upper arc of arched lining to mitigate potential lining damage under BLEVE load.

(2) Based on crack grades, the linings at the corner and upper arc of arched tunnel subjected to the considered internal BLEVE experience severe damage and moderate damage, respectively. Compared to BLEVE, its equivalent TNT explosion load with the same energy release can induce the collapse-level damage of arched lining. Peak and residual strain energies of arched lining subjected to the TNT equivalency explosion load are 83.4% and 380% higher than those subjected to BLEVE load. Therefore, it is too conservative to predict the structural response of the tunnel subjected to BLEVE by using the TNT equivalency load.

(3) Compared to increasing the reinforcement ratio, increasing concrete grade and thickness and enhancing surrounding rock mass stiffness can more effectively mitigate the damage of arched lining subjected to internal BLEVE.

(4) In view of the damage level and average strain energy of lining, the arched lining with the concrete strength equal to or higher than 25 MPa and the lining thickness not less than 600 mm and surrounded by rock mass with the stiffness over 45 GPa experiences only moderate or slight damage subjected to the BLEVE scenario considered in this study (i.e., the worst BLEVE scenario induced by a 20 m^3 LPG tanker explosion), therefore satisfying the BLEVE-resistant performance of the arched tunnel.

(5) The study mainly considers the structural response of tunnel against internal BLEVE overpressures. The effects of possible fireball and the projectile of tanker fragments on the tunnel response will be investigated in another study.

Declaration of Competing Interest

The authors declare that they have no known competing financial interests or personal relationships that could have appeared to influence the work reported in this paper.

Acknowledgements

The authors acknowledge the financial support from the Australian Research Council (ARC) via Australian Laureate Fellowship (FL180100196).

Reference

Austroads, 2019. Guide to road tunnels part 2: Planning, design and commissioning, AGRT02-19.

Birk, A. M., Eyssette, R., Heymes, F., 2019. Early moments of BLEVE: From vessel opening to liquid flashing release. Process Saf. Environ. Prot. 132, 35-46.

Blair, D. P., 2015. The free surface influence on blast vibration. Int. J. Rock Mech. Min. Sci. 77, 182-191.

Bresler, B., Pister, K. S., 1958. Strength of concrete under combined stresses. Journal of ACI 55, 321-345.

Bubbico, R., Marchini, M., 2008. Assessment of an explosive LPG release accident: a case study. J. Hazard. Mater. 155, 558-565.

Chaudhary, R.K., Mishra, S., Chakraborty, T., Matsagar, V., 2018. Vulnerability analysis of tunnel linings under blast loading. Int. J. Prot. Struct. 10, 73-94.

Chen, W.S., Hao, H., Chen, S.Y., 2015. Numerical analysis of prestressed reinforced concrete beam subjected to blast loading. Mater. Des. 65, 662-674.

Cheng, R.S., Chen, W.S., Hao, H., Li, J.D., 2021. A state-of-the-art review of road tunnel subjected to blast loads. Tunn. Undergr. Space Technol. 112.

Cotsovos, D. M., Stathopoulos, N. D., Zeris, C. A., 2008. Behavior of RC beams subjected to high rates of concentrated loading. J. Struct. Eng. 134, 1839-1851.

Cui, J., Hao, H., Shi, Y.C., 2017. Discussion on the suitability of concrete constitutive models for high-rate response predictions of RC structures. Int. J. Impact Eng. 106, 202-216.

Eyssette, R., Heymes, F., Birk, A. M., 2021. Ground loading from BLEVE through small scale experiments: Experiments and results. Process Saf. Environ. Prot. 148, 1098-1109.

Feldgun, V. R., Karinski, Y. S., Yankelevsky, D. Z., 2014. The effect of an explosion in a tunnel on a neighboring buried structure. Tunn. Undergr. Space Technol. 44, 42-55.

Gao, M., Wang, Y., Gao, G. Y., Yang, J., 2013. An analytical solution for the transient response of a cylindrical lined cavity in a poroelastic medium. Soil Dyn. Earthq. Eng. 46, 30-40.

Goel, M. D., Verma, Shivani, Panchal, Sandeep, 2020. Effect of Internal Blast on Tunnel Lining and Surrounding Soil. Indian Geotech. J.

Hao, H., Hao, Y.F., Li, J., Chen, W.S., 2016. Review of the current practices in blast-resistant analysis and design of concrete structures. Adv. Struct. Eng. 19, 1193-1223.

Hao, Y.F., Hao, H., 2014. Influence of the concrete DIF model on the numerical predictions of RC wall responses to blast loadings. Eng. Struct. 73, 24-38.

Hemmatian, Behrouz, Planas, Eulàlia, Casal, Joaquim, 2017. Comparative analysis of BLEVE mechanical energy and overpressure modelling. Process Saf. Environ. Prot. 106, 138-149.

Hendron, A. J., 1977. Engineering rock blasting in civil projects. Structural and Geotechnical Mechanics: A Volume Honouring Nathan M. Neumark, Prentice Hall, Englewood Cliffs.

Huo, X.F., Shi, X.Z., Qiu, X.Y., Zhou, J., Gou, Y.G., Yu, Z., Ke, W.Y., 2020. Rock damage control for large-diameter-hole lateral blasting excavation based on charge structure optimization. Tunn. Undergr. Space Technol. 106.

Kristoffersen, M., Minoretti, A., Børvik, T., 2019. On the internal blast loading of submerged floating tunnels in concrete with circular and rectangular cross-sections. Eng. Fail. Anal. 103, 462-480.

Krone, E., 2018. Internal blast loading of submerged floating tunnels in concrete. Norwegian University of Science and Technology, Trondheim.

Lai, H., Wang, S., Xie, Y., 2016. Study on the Fire Damage Characteristics of the New Qidaoliang Highway Tunnel: Field Investigation with Computational Fluid Dynamics (CFD) Back Analysis. Int. J. Environ. Res. Public Health 13.

Lemmon, E.W., Huber, M.L., McLinden, M.O., 2007. NIST Reference Fluid Thermodynamic and Transport Properties—REFPROP Version 8.0. User's Guide. National Institute of Standards and Technology, Physical and Chemical Properties Division, Boulder, Colorado.

Li, J., Hao, H., Wu, C.Q., 2017. Numerical study of precast segmental column under blast loads. Eng. Struct. 134, 125-137.

Li, J.D., Hao, H., 2020. Numerical study of medium to large scale BLEVE for blast wave prediction. J. Loss Pre.v Process Ind. 65.

Li, Jingde, Hao, Hong, Chen, Wensu, Cheng, Ruishan, 2021. Calculation of BLEVE energy and overpressures inside a tunnel using analytical and CFD methods. Tunn. Undergr. Space Technol. 104263.

Liu, K., Li, Q.Y., Wu, C.Q., Li, X.B., Li, J., 2018. A study of cut blasting for one-step raise excavation based on numerical simulation and field blast tests. Int. J. Rock Mech. Min. Sci. 109, 91-104.

Liu, K.W., Li, X.D., Hao, H., Li, X.B., Sha, Y.Y., Wang, W.H., Liu, X.L., 2019. Study on the raising technique using one blast based on the combination of long-hole presplitting and vertical crater retreat multiple-deck shots. Int. J. Rock Mech. Min. Sci. 113, 41-58.

Livermore Software, Technology, 2020. LS-DYNA keyword user's manual, R12.

Malvar, L.J., 1998. Review of static and dynamic properties of steel reinforcing bars. ACI Mater. J. 95, 609-614.

Ministry of Transport of the People's Republic of China, 2018. Specifications for design of highway tunnels section 1 Civil engineering, JTG 3370.1-2018.

Molenaar, D.J., Weerheijm, J., Vervuurt, A., Burggraaf, H., Roekaerts, D., Meijers, P., 2009. Bijzondere belastingen in tunnels: Eindrapport, TC211-05-09.

Mussa, Mohamed H., Mutalib, Azrul A., Hamid, Roszilah, Naidu, Sudharshan R., Radzi, Noor Azim Mohd, Abedini, Masoud, 2017. Assessment of damage to an underground box tunnel by a surface explosion. Tunn. Undergr. Space Technol. 66, 64-76.

Olav, R. H., Kjellander, M., 2016. CFD modelling of blast waves from BLEVEs. Chem. Eng. Trans. 48, 199-204.

Planas-Cuchi, E., Salla, J. M., Casal, J., 2004. Calculating overpressure from BLEVE explosions. J. Loss Pre.v Process Ind. 17, 431-436.

Prugh, R. W., 1991. Quantitative Evaluation of "Bleve" Hazards. J. Fire Prot. Eng. 3, 9-24.

Qian, Haimin, Li, Jun, Zong, Zhouhong, Wu, Chengqing, Pan, Yahao, 2021a. Behavior of precast segmental utility tunnel under ground surface Explosion: A numerical study. Tunn. Undergr. Space Technol. 115.

Qian, Haimin, Zong, Zhouhong, Wu, Chengqing, Li, Jun, Gan, Lu, 2021b. Numerical study on the behavior of utility tunnel subjected to ground surface explosion. Thin-Walled Structures 161.

Shi, Y.C., Li, Z.X., Hao, H., 2008. Mesh size effect in numerical simulation of blast wave propagation and interaction with structures. Trans. Tianjin Univ. 14, 396-402.

Strehlow, R. A., Luckritz, R. T., Adamczyk, A. A., Shimpi, S. A., 1979. The blast wave generated by spherical flames. Combust. Flame 35, 297-310.

Tiwari, R., Chakraborty, T., Matsagar, V., 2016. Dynamic Analysis of Tunnel in Weathered Rock Subjected to Internal Blast Loading. Rock Mech. Rock Eng. 49, 4441-4458.

US Department of Defense, 2008. Structures to resist the effects of accidental explosions, UFC 3-340-02.

US Department of Transportation Federal Highway Administration, 2009. Technical manual for design and construction of road tunnels — civil elements, FHWA-NHI-10-034.

Van den Berg, A. C., Van der Voort, M. M., Weerheijm, J., Versloot, N. H. A., 2006. BLEVE blast by expansion-controlled evaporation. Process Saf. Prog. 25, 44-51.

Vervuurt, A. H. J. M., Galanti, F. M. B., Wubs, A. J., Van den Berg, A. C., 2007. Effect of explosions in tunnels-Preliminary assessment of the structural response, 2007-D-R0156/A.
Wang, G.H., Wang, Y.X., Lu, W.B., Zhou, W., Chen, M., Yan, P., 2016. On the determination of the mesh size for numerical simulations of shock wave propagation in near field underwater explosion. Appl. Ocean Res. 59, 1-9.
Wang, G.H., Zhang, S.R., 2014. Damage prediction of concrete gravity dams subjected to underwater explosion shock loading. Eng. Fail. Anal. 39, 72-91.
Wang, W., Zhang, D., Lu, F.Y., Wang, S.C., Tang, F.J., 2012. Experimental study on scaling the explosion resistance of a one-way square reinforced concrete slab under a close-in blast loading. Int. J. Impact Eng. 49, 158-164.
Wu, C., Lu, Y., Hao, H., Lim, W. K., Zhou, Y., Seah, C. C., 2003. Characterisation of underground blast-induced ground motions from large-scale field tests. Shock Waves 13, 237-252.
Wu, C.Q., Lu, Y., Hao, H., 2004. Numerical prediction of blast-induced stress wave from large-scale underground explosion. Int. J. Numer. Anal. Methods Geomech. 28, 93-109.
Xie, L. X., Lu, W. B., Zhang, Q. B., Jiang, Q. H., Chen, M., Zhao, J., 2017. Analysis of damage mechanisms and optimization of cut blasting design under high in-situ stresses. Tunn. Undergr. Space Technol. 66, 19-33.
Yang, G.D., Wang, G.H., Lu, W. B., Yan, P., Chen, M., 2019. Damage assessment and mitigation measures of underwater tunnel subjected to blast loads. Tunn. Undergr. Space Technol. 94.
Yang, H.J., 2006. Deformation characteristic of tunnel surrounding rock under complex conditions. J. Railw. Eng. Soc. 1, 57-60.
Zaid, Mohammad, Sadique, Md Rehan, 2020. Blast resistant behaviour of tunnels in sedimentary rocks. Int. J. Prot. Struct.
Zhou, Y., Zhao, J., Chong, K., Seah, C. C., 2002. Dynamic response and tunnel damage from explosion loading, Proc. international symposium on defence construction, Singapore.
Zhou, Y.X., 2011. Earthquakes as a rock dynamic problem and their effects on rock engineering structures, Advances in Rock Dynamics and Applications. Taylor and Francis Group, London, pp. 457-481.
Zhou, Y.X., Jenssen, A., 2009. Internal separation distances for underground explosives storage in hard rock. Tunn. Undergr. Space Technol. 24, 119-125.